Charles University
Faculty of Science
Institute of Hydrogeology, Engineering Geology and Applied Geophysics
Study Programme Applied Geology, Specialization Applied Geophysics

Analysis of volcanic tremor during the 2021 Fagradalsfjall eruption

Analýza vulkanického tremoru během erupce sopky Fagradalsfjall, 2021

Master's thesis

Bc. František Sova
Supervisor: prof. RNDr. Tomáš Fischer, PhD
Prague 2022

I declare hereby that I made this dissertation thesis by myself and that I mentioned and cited properly all the sources and literature. At the same time, I declare that this thesis was not used to obtain another or the same title.

Prague, 10th May 2022

Bc. František Sova

Abstract

Volcanic tremors are low frequency seismic events, occurring prior to or during eruptions and are believed to be caused by the movement of magma. The study of those events can reveal subsurface processes during volcanic activity, furthermore it can help to reconstruct eruptions, which cannot be observed directly.

The presented study describes the volcanic tremor during the 2021 Fagradalsfjall eruption in Iceland. Seismic data from several stations were processed to produce a half-year record of volcanic activity. Additionally, the tremor amplitude attenuation was investigated.

The seismic record was marked by a reoccurring tremor signal in the frequency band 1-10 Hz, which temporally matched with the different phases of effusive eruption. Its amplitudes varied in time, showing three distinct patterns. The weak continuous tremor in the first weeks of eruption transitioned into regular pulses, lasting several minutes, and later into a different pulsation with a 1.5-day period. Those variations might reflect the changes in geometry and magma flow of the underground magmatic system.

Abstrakt

Vulkanické tremory jsou nízkofrekvenční seismické jevy, které se vyskytují před nebo během sopečných erupcí a souvisí s pohybem magmatu pod povrchem. Jejich studium pomáhá odhalit podpovrchové procesy během sopečné činnosti, navíc může pomoci rekonstruovat erupce, které nemohou být pozorovány přímo.

Předkládaná studie popisuje vulkanický tremor během erupce sopky Fagradalsfjall na Islandu v roce 2021. Seismická data z několika stanic byla zpracována tak, aby vznikl záznam půlroční vulkanické činnosti. Kromě toho byl zkoumán útlum amplitudy tremorů s rostoucí vzdáleností od zdroje.

Půlroční záznam se vyznačoval signálem opakujícího se tremoru ve frekvenčním pásmu 1-10 Hz, který časově odpovídal jednotlivým fázím efuzivní erupce. Jeho amplituda se s časem měnila a bylo možné rozlišit tři vzorce. Na počátku se vyskytující slabý kontinuální tremor se změnil v pravidelné několikaminutové pulzy, které přerostly v delší, jeden a půl dne trvající pulzy. Tyto variace mohou být odrazem změn v geometrii a proudění magmatu podzemního magmatického systému.

I would like to thank my supervisor prof. RNDr. Tomáš Fischer, PhD for his constant support, guidance and interesting ideas. Also, I would like to thank MSc. Ali Salama, who shared his Python expertise with me and helped with the encountered problems. Last but not least I would like to thank doc. RNDr. Jan Vilhelm, CSc. and Mgr. Josef Vlček, PhD. for their advice.

Prague, 10th May 2022

Bc. František Sova

Contents

1 Introduction

Volcanic activity and its associated processes can have a severe impact on human lives and infrastructure. Therefore many prediction and observation methods have evolved to forecast the scope and occurrence of volcanic events. One of the common techniques is seismic monitoring, which helps to assess the risks in real time. Additionally it allows creation of prediction models using the probability statistics on the past records. Furthermore the analysis of recorded seismic signals can broaden the knowledge of volcanic systems and their parts, that cannot by directly observed (e.g. in remote locations, in the subsurface).

Volcanic eruptions are accompanied by various seismic events, making the recorded signal complex. Apart from the more distinct events like high frequency earthquakes and explosions, there are also other, less prominent ones, including tremors and low-frequency earthquakes (Zobin, 2003). While earthquakes are the main topic in seismology, volcanic tremors, as much weaker signals, receive less attention in the research. One of the challenges when studying volcanic tremors is their widely varying signature, which complicates the automated detection as well as the modelling of the source. Additionally, such diverse signal might be confused with events of non-volcanic origin (Eibl et al., 2015).

There have been long time efforts to explain the origin of volcanic tremors and to derive some generally applicable laws, but only with limited success. It is not a simple mechanism as a brittle fracture, but rather a complex interplay between the bedrock, rising magma and exsolved gases (Konstantinou & Schlindwein, 2002).

This study offers an overview of volcanic tremors. It investigates their occurrences, their relation to magmatic eruptions and their possible sources. The theoretical section is complemented by a case study from 2021 Fagradalsfjall eruption in Iceland, which was closely observed by the scientific community worldwide.

The first part provides the basics of seismology and signal processing. It is followed by the definition of tremors and by an overview of related studies. The third part characterizes the location of the volcano and its specific tectonic settings. Further it describes the precursors and events during the eruption. The seismic data acquisition, data format and processing methods are given in part four. The preliminary and final results are presented in the next part. They include tremor characterization during half a year of activity and analysis of the amplitude attenuation between different stations. The last part is the evaluation of results and their comparison with other documented cases.

2 Seismological concepts

2.1 Seismic waves

Seismic methods are based on deriving information from the recorded seismic waves. Those waves are a type of mechanical waves, which travel through the subsurface and cause particle displacement. They spread spherically from the point of origin, until all their energy is transferred. The energy propagates in the form of body waves, which are partially converted into surface waves upon arrival at the free surface boundary.

In the vicinity of the seismic source, permanent deformation occurs, while further in the field the deformation is elastic. Ground particles are displaced, but after some time they return to their original positions, creating a harmonic motion, which is recorded.

Based on the particle motion direction (polarization), body waves can be divided into the compressional P-waves and transverse S-waves. P-waves are polarized in the direction of propagation and they are the first incoming waves recorded on seismograms. S-waves can be horizontally (SH) or vertically polarized (SV) in the plane perpendicular to the propagation axis and are recorded later (Lowrie, 2007).

The relations between the body wave velocities and the properties of the propagation media are

$$V_p = \sqrt{\frac{\lambda+2\mu}{\rho}}, \qquad V_s = \frac{\mu}{\rho}.$$

V_p is the P-wave velocity, V_s is the S-wave velocity, λ is Lamé's first parameter, μ is Lamé's second parameter (also known as shear modulus) and ρ is the density. In liquids, the shear modulus equals zero, setting the S-wave velocity to zero. Therefore S-waves propagate only through solid media. Despite the seemingly inverse relationship between the velocities and material density, seismic waves propagate faster in denser materials. This is due to a greater increase of Lamé's coefficients with higher density (Everett, 2013).

Based on the average mechanic properties of rocks, the V_p/V_s ratio is approximately 1.7. Vice versa, if the velocity ratio is known from a seismic measurement, the relevant rock properties can be estimated (Alsadi, 2016).

Surface waves propagate slower than body waves, arriving on seismograms later. They are usually stronger as their energy is less attenuated in the subsurface. The propagation velocity depends on their frequencies and their periods can be longer than 10 s.

The two main types of surface waves are Rayleigh and Love waves, each with a different polarization. Outside of earthquake events, they are visible on the seismic record as the omnipresent Earth's activity, which is referred to as microseisms. The source of microseisms is the motion of masses in the atmosphere and ocean, which makes the signal stronger in coastal areas. In the frequency spectra from 100 global seismic stations, the main characteristic peak of microseisms is between the periods of 5-8 s (Fig. 2.1). Although this low frequency signal is usually regarded as noise, it can be used in the study of Earth's structure (Shearer, 2009).

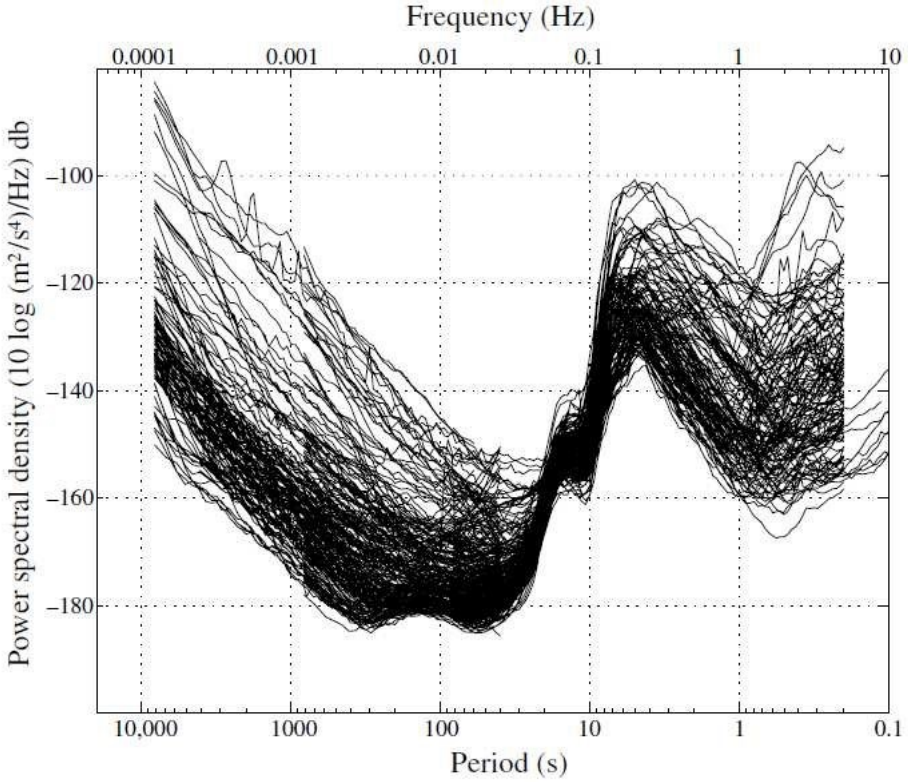

Figure 2.1: *Acceleration spectra showing the average global seismic noise levels. The spectra were computed in intervals between earthquakes from the signal at over 100 seismic stations. There is a peak at 5-8 s period, typical for the microseismic noise (source: Shearer, 2009).*

The decreasing energy of seismic signal, when traveling through a medium, is called attenuation. The biggest reduction of energy is due to the geometrical spreading from a point source. The propagating wavefront has a half-sphere surface area equal to $2\pi r^2$, which increases with time.
In a certain distance r from the source, the energy E is spread over larger area. The energy density I of body waves is then defined as

$$I(r) = \frac{E}{2\pi r^2}.$$

If the energy density is averaged over a complete harmonic cycle, its relation to amplitude A is

$$I_{av} = \frac{1}{2}\rho\omega^2 A^2 .$$

When both equations are combined, the energy E is proportional to the squared amplitude

$$E \sim A^2,$$

and the distance r is inversely proportional to the amplitude

$$1/r \sim A .$$

The amplitude decrease of body waves due to the geometrical spreading is then governed by the factor of $1/r$. Because surface waves propagate differently from body waves, their geometrical factor is also different. Their wavefront can be viewed as a circle with a perimeter of $2\pi r$ and their amplitude then decreases with distance r only by a factor of $1/\sqrt{r}$ (Lowrie, 2007).

Another source of attenuation are the imperfect properties of particles, that do not behave completely elastically. Some of the energy is absorbed due to friction and transformed into heat. This loss is referred to as the anelastic attenuation and can be described by a dimensionless quality factor Q, which is defined as the energy loss $-\Delta E$ per cycle

$$\frac{1}{Q(\omega)} = -\frac{\Delta E}{2\pi E}$$

High Q factor means that the intrinsic attenuation is small. In the distance x from the source, the amplitude decrease caused by the anelastic attenuation is

$$A(x) = A_0 e^{-\omega x/2cQ}$$

Where ω is the angular frequency and c is the wave velocity. It is clear from this relation, that the anelastic attenuation is dependent on frequency. Higher frequencies will attenuate faster and cause the Earth to behave as a low-pass filter (Shearer, 2009).

In real conditions, the energy of seismic wave is also partitioned on boundaries and heterogeneities by diffraction. When this scattering is neglected, geometrical spreading and anelastic attenuation can be combined into

$$A(r) = A_0 \left(\frac{r_0}{r}\right) e^{\alpha(r_0 - r)}$$

describing the amplitude decrease at distance r from the source.

The α is the attenuation coefficient, which is related to the quality factor Q by (Everett, 2013)

$$\alpha = \frac{\omega}{2cQ}$$

2.2 Earthquakes and their parameters

Earthquakes are abundant in the areas around plate boundaries, where their sources are sudden movements of tectonic plates. Even though a small number of earthquakes is caused by volcanic activity, most of them are related to tectonic processes, which can be categorized based on the relative movement of adjacent blocks. The slip angle or rake λ is the angle between the direction of the movement and the fault line measured in the fault plane. Based on the rake, it is possible to distinguish left-lateral (λ = 0°) and right lateral (λ = 180°) strike-slips, normal fault (λ = −90°) and reverse fault (λ = 90°) (Fig. 2.2; Kayal, 2006; Lowrie, 2007).

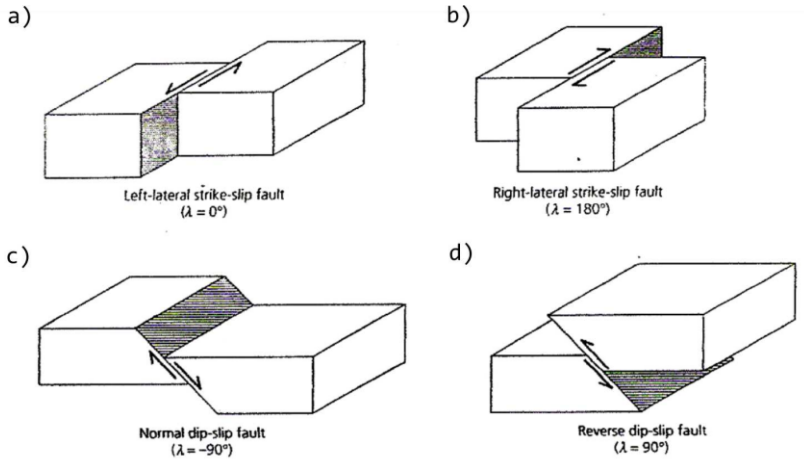

Figure 2.2: *Four different types of fault movement, including the left-lateral strike-slip (a), right-lateral strike-slip (b), normal fault (c) and reverse fault (d)(Adapted from: Kayal, 2006)*

Movement along a fault can be modelled, in the simplest form, as a pair of body forces acting in opposite directions. These vector dipoles are perpendicular to each other and altogether form so-called double couple source. Inherently, the solution for double couple model is two fault planes perpendicular to each other. The actual plane is usually called the primary plane, while the perpendicular plane is called the auxiliary plane. This ambiguity must be resolved with the help of other markers, like the rupture orientation or location of aftershocks (Shearer, 2009).

All the forces present in a seismic source can be described by the moment tensor $\boldsymbol{M}$, which provides solution for a given focal mechanism. It can be decomposed into the sum

$$\boldsymbol{M} = \boldsymbol{M}^{0} + \boldsymbol{M}^{DC} + \boldsymbol{M}^{CLVD}.$$

Apart the double couple part $\boldsymbol{M}^{DC}$, it also consists of two other components, which represent different types of mechanisms (Fig. 2.3). One of them is the isotropic part $\boldsymbol{M}^{0}$, which expresses volume changes in the source and is connected to explosions. The residual deviatoric part $\boldsymbol{M}^{CLVD}$ is called the Compensated Linear Vector Dipole (CLVD) and does not have a clear physical representation. Both of the non double-couple parts are common during magma injections, volcano eruptions or landslides (Shearer, 2009).

The moment tensor $\boldsymbol{M}$ can be used to derive the scalar seismic moment M_0 following the expression

$$M_0 = \frac{1}{\sqrt{2}}\left(\sum_{ij} M_{ij}^2\right)^{1/2}.$$

The seismic moment is given in newton-meters (Nm) and serves as the main parameter of earthquakes' strength and size. Using it further in equation

$$M_0 = \mu D A$$

it is possible to estimate the average displacement on the fault D and its area A, given the shear modulus μ (Shearer, 2009).

The scalar seismic moment is also used for computing the moment magnitude M_w, which is the most accurate estimate of an earthquake size. Unlike other magnitude scales, it does not saturate for strong events. Magnitude saturation results in underestimating high-energy earthquakes (Kayal, 2006). If the seismic moment M_0 is given in newton-meters, the moment magnitude M_w can be computed using the formula (Lowrie, 2007)

$$M_w = \frac{2}{3}(log_{10}M_0 - 9.1).$$

Locating the source of an earthquake is done by picking the first arrivals of P-waves and/or S-waves on multiple seismic stations. The parameters of the origin (x_0, y_0, z_0, t_0) are computed using a non-linear inverse problem from the known arrival times t_i and the station coordinates x_i, y_i, z_i. A velocity model is used to calculate the arrival times from a chosen origin and then the residuals between the modelled and measured arrival times are computed. The inverse problem seeks to minimize those residuals (Shearer, 2009).

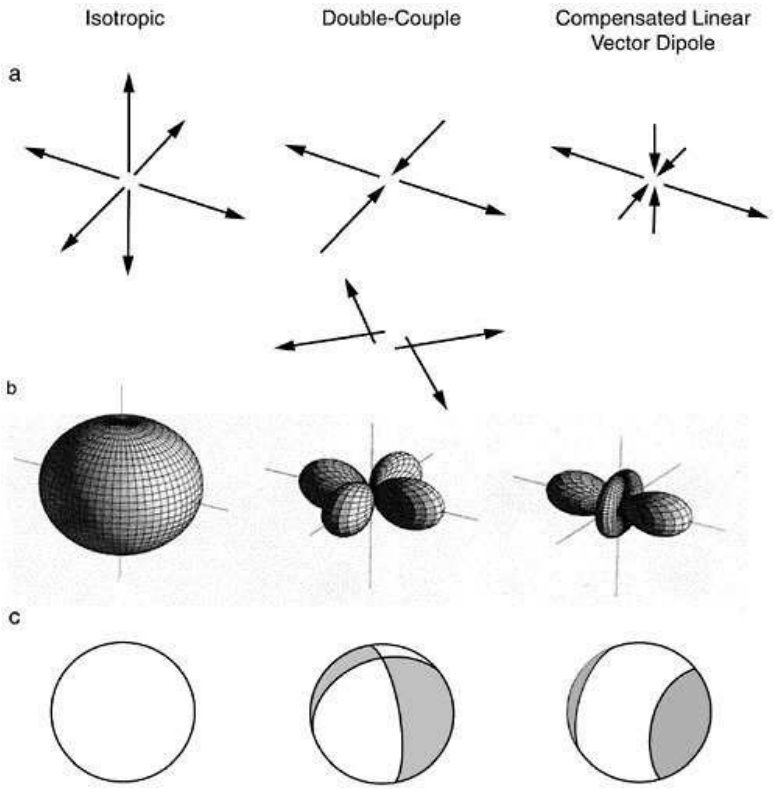

Figure 2.3: *Graphic representations of the moment tensor components. Isotropic part, Double-couple and Compensated Linear Vector Dipole are shown as vector forces (a), 3D model (b) and a beach ball projection (c)(source: Living on an Active Earth: Perspectives on Earthquake Science. The National Academies Press, 2003).*

There are various location methods, including linearized iterative methods or non-linear methods implementing grid searches. To find the minimum residual of misfit, two norms are used. The L1 norm

$$\epsilon = \sum_{i=1}^{n} |t_i - t_i^p|$$

uses the sum of the absolute differences and the L2 norm

$$\epsilon = \sum_{i=1}^{n} [t_i - t_i^p]^2$$

uses the least squares (n is the number of stations, t_i are the predicted and measured arrival times). The L1 norm is more robust, which means that it is not so much affected by outliers (Shearer, 2009). Despite its robustness, it has a high

computational cost, therefore the L2 norm is preferred. The effect of outliers in L2 can be minimized using weighting.

The location error can be estimated by computing the standard deviation of the residuals and determining the confidence interval for the location. The main error stems from the inaccurate determination of the wave first arrivals. The location uncertainty also increases in the scenario, that all of the seismic stations are in one direction from the source. Also it increases, if there are many lateral discontinuities in between (Shearer, 2009).

2.3 Seismometers

The traveling seismic waves are recorded by seismometers. The output of those instruments is proportional to the velocity, displacement or acceleration of the ground. The measurement is usually done in 3 orthogonal directions, covering both horizontal and vertical components of seismic waves. The difference between the smallest and the highest measurable signal amplitude is the seismometer's dynamic range and is given in decibels [dB].

Modern devices consist of a suspended mass inside a frame, which is fixed to the ground. The mass stays in place due to inertia and its relative movement to the frame is measured. The relation between the ground velocity and the mass velocity is expressed by the instrument response function. In the case of electromagnetic seismometers, the mass is a magnet and the frame is a coil (Shearer, 2009). To achieve greater dynamic ranges, some seismometers have a negative feedback loop, which keeps the mass motionless relative to the frame by applying electromagnetic force (Teupser & Plešinger, 1979). The output voltage is directly proportional to the ground motion (seismometer's gain) and it is further converted into counts using an AD digitizer (Shearer, 2009).

Seismometers can be divided into short and long-period seismometers. The separation line is the main frequency of microseisms between 0.1-1.0 Hz. The division stems from a difficulty to produce a flat amplitude response in a broad range of frequencies. If the frequency response is not flat, signals are distorted and not proportionate to the measured quantity. More advanced seismometers are broadband, which means that they have a flat response for both short and long period events (Shearer, 2009).

2.4 Format of seismic data

Seismic data are usually stored in the international SEED (Standard for the Exchange of Earthquake Data) format, which is intended for station and event-oriented time series, sampled in even intervals. It was developed for an easier exchange of seismic data between institutions. Nowadays it is used on all levels of

data handling from the recording unit to the end user. Over time the format has become convenient also in other ground-based observations in different geosciences (e.g. strain, gravimetric, magnetic data).

There are two basic forms of SEED - one handling the dataless metadata, containing information about the station and channels, while the other consists solely of the waveform files. This type is called miniSEED and it has a fixed-size header with a limited metadata and requires, that the operator is familiar with the specification of the seismic network. The data are recorded usually in lengths of 512-byte segments, which are later concatenated into so-called "streams". They typically contain records from one channel, although multiplexing is also a possibility (Ahern et al., 2009).

Seismic channels are specified by the network and station identification and by three-letter code, referring to the band, used instrument and orientation. For example, the CHZ channel in REYKJANET network, which was used in this study, has C referring to the sample rate between 250-1000 Hz and the corner frequency higher than 10 s. The H refers to High Gain Seismometer and Z stands for the vertical component (Ahern et al., 2009). An example of complete channel identification from REYKJANET network could be 7E.LAT..CHE, where 7E is the network code, LAT is the abbreviation of Látur station and CHE is the corresponding horizontal W-E channel.

The end user usually does not need to understand the structure of SEED files, in order to write or read them. There is *libmseed* C library facilitating the data manipulation. Python, where most of the data processing in this study was done, has an equivalent of *libmseed* library. It is included in the *ObsPy* seismological framework, wrapped in one of its modules. *ObsPy* is a versatile toolbox, that offers processing and simple plotting functions. In comparison to other seismological software, it is open-source and allows access to a full programming language (Beyreuther et al., 2010).

MiniSEED data in *ObsPy* are loaded into a Stream object, including one or multiple Trace objects. Each of the Trace objects represents continuous waveform data and has its data attribute, alongside with stats attribute, containing meta-information. The meta-information includes the SEED channel identification and other parameters. Based on the identifier it is possible to merge Traces together and apply some processing methods (Krischer et al., 2015).

2.5 Signal processing techniques

Recorded seismic signals contain information, that can be extracted by different processing methods. One of the main concepts in signal processing is the Fourier Transform, which demonstrates, that any variable function (signal) is in fact a

superposition of several frequency components. It converts the signal from its time domain to the frequency domain by

$$F(\omega) = |F(\omega)|e^{i\Phi(\omega)} = \int_{-\infty}^{\infty} f(t)e^{-i\omega t}dt$$

where $F(\omega)$ is the complex Fourier transform consisting of the amplitude spectrum $|F(\omega)|$ and the phase spectrum $\Phi(\omega)$.

Because most of the data is in a digital form and processed by computers, a version of the FT called the Discrete Fourier Transform (DFT) is used. Following the expression

$$X(\omega_k) \triangleq \sum_{n=0}^{N-1} x(t_n)e^{-i\omega_k t_n}, \qquad k = 1,2,3,\dots,N-1,$$

it sums the signal amplitudes $x(t_n)$ of specific frequency component ω_k over a discrete number of N sampling instants (Bormann & Wielandt, 2013). The value X is the Fourier coefficient and it is a complex value (Everett, 2013).

The computation of DFT is usually implemented by the Fast Fourier Transform (FFT) algorithm, which means that FFT and DFT are used nearly interchangeably. The FFT is used for broad-band sampled signals with finite length (Bormann & Wielandt, 2013).

The signal sampling frequency f_S (sampling rate) is the number of points per unit of time, usually given in points per second or hertz [Hz]. The sampling rate limits the maximum frequency that can be accurately recorded and retrieved from a signal. This frequency is called the Nyquist frequency and it is equal to $f_S/2$. It is the upper limit of the frequency domain, as any signal component with higher or equal frequency is in the FT shifted below the Nyquist frequency and causes distortion. This is the unwanted effect of aliasing. Therefore anti-alias filters are applied to the signal before digitization (Everett, 2013).

The resolution in the frequency domain is given by

$$\Delta f = f_S/N$$

where N is the number of points in the time domain. Multiples of Δf are referred to as frequency bins.

The FFT produces a two-sided spectrum in a complex form, which has to be converted to a one-sided spectrum using the range below the Nyquist frequency. By squaring the amplitude (magnitude) spectrum, a power spectrum (also called PSD - Power Spectral Density) can be obtained (Cerna & Harvey, 2000).

In the FFT computation, the resolution in the frequency domain Δf does not need to correspond to an integral cycle of the signal. In this case, the energy from the non-integral frequency component is spread over several frequency bins in the

spectrum and spectral leakage occurs. It causes amplitude inaccuracy and makes closely spaced spectral peaks less distinct.

To avoid the distortion, differently shaped windows are used. They are applied by convoluting their spectra with the spectrum of the signal. The most common ones are the Hann (Hanning) window, Blackman window and Hamming window. All of them are cosine-sum windows and their spectra are characterized by a central peak with side lobes (Fig. 2.4). The Hann window is used in the majority of cases, because it substantially reduces the spectral leakage and it has a good frequency resolution (Cerna & Harvey, 2000).

Window functions are also required for plotting spectrograms using another variant of the FT. The Short-time Fourier Transform (SFT) is a series of FFTs computed in windowed time segments, which can overlap. The resulting magnitudes are then plotted as intensities in a logarithmic scale (Smith, 2007).

A typical logarithmic unit is decibel [dB], which expresses the dimensionless ratio of a measured and reference value. The power (energy) ratio in dB is given by

$$dB = 10log\frac{P}{P_r},$$

The energy is proportional to the squared amplitude A^2. Because squaring the ratio is the same as multiplying the expression by 2, a different formula

$$dB = 20log\frac{A}{A_r},$$

is used for the amplitude ranges. Using decibels is practical for large dynamic ranges, which is often the case in seismic measurement and processing (Cerna & Harvey, 2000).

When working in the frequency domain, the signal can be easily filtered, cutting off range of certain frequencies. It is used for improving the signal-to-noise (SNR) ratio of target component, while suppressing the noise and other frequency components. Filtration convolves the signal with a specific filter function with a sharp frequency cut-off and flat response in the target range. Such function is not physically realizable, therefore a compromise must be chosen. There are several filters, including the Butterworth filter, which has the flattest response in the passband. Filters can be divided based on their frequency ranges into low-pass, high-pass and bandpass filters (Everett, 2013).

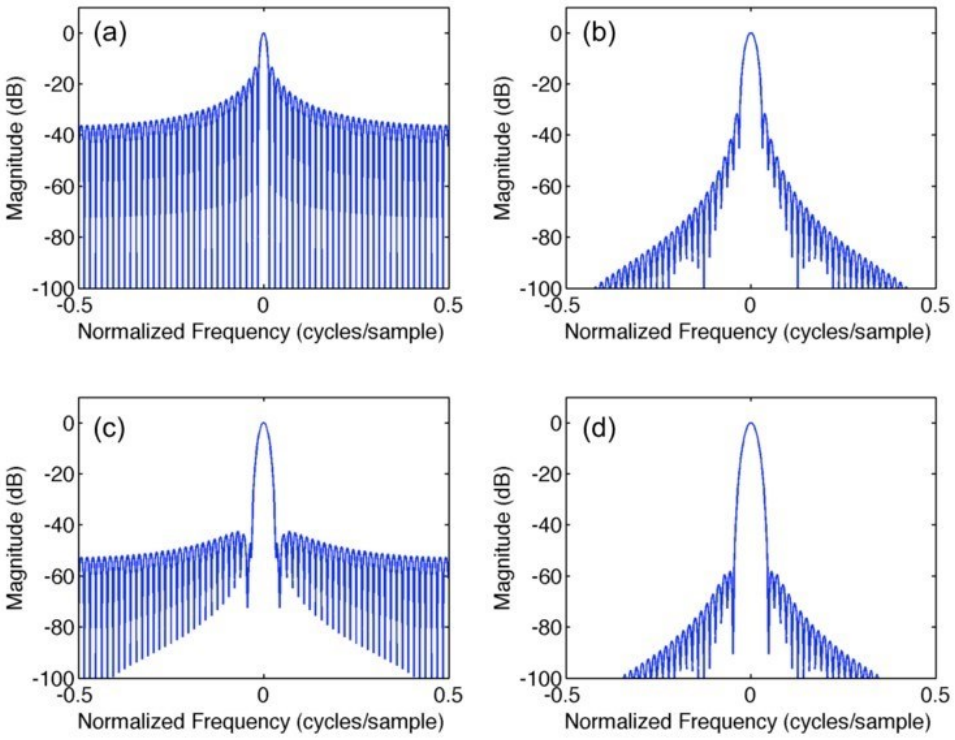

Figure 2.4: *Most common window functions used in signal processing: Boxcar (a), Hann (b), Hamming (c), and Blackman (d). All of them have a central peak and side lobes (source: Ao & Dolan, 2022, SIRHEN: A data reduction program for photonic Doppler velocimetry measurements).*

3 Volcanic tremors

3.1 Seismicity of volcanic eruptions

Following the definition given by Global Volcanism Program, a volcano is an accumulation of explosively or effusively erupted materials originating from single or multiple vents or fissures at the surface of the Earth or other planets. Around 50 volcanoes worldwide are erupting at any given moment, with some eruptions lasting up to several years. Their activity is being monitored by seismic measurements, as well as by other methods including ground motion, gas release or gravimetric measurements.

While some volcanoes have one main dominant edifice, others are part of larger volcanic systems. They can be comprised of features like vents, maars, cinder cones and lava fields. They share the same magmatic source and can be hundreds of kilometres in size (Global Volcanic Program, 2013).

Volcanic eruptions are accompanied by seismic activity, which has various signatures and sources. It ranges from volcanic tremors and low frequency events to explosion and tectonic earthquakes (McNutt, 1992). While the high frequency events exhibit distinct amplitude changes, including the first arrival of P- and S-waves, the onset of events at lower frequencies is more blurred (Permana et al., 2022). Therefore, the conventional source locating method using the arrival times might not be applicable to them. One alternative method is to use the amplitude decay with distance from the source, assuming the isotropic spreading of the wavefront. Finding the true locations of the events is important for tracking the changes in the subsurface and understanding the respective volcanic processes (Benediktsdóttir et al., 2022).

3.2 Observed tremors

While volcano-tectonic earthquakes are connected to a fault movement, brittle rock failure or dike propagation, tremor sources are more ambiguous (Konstantinou & Schlindwein, 2003). Their characteristics vary between locations, but also between eruptions in one place, which complicates the formulation of general laws. Several models were proposed to explain the source of tremor signal, including continuous gas bursting, a resonating pipe filled with fluid or repeating occurrence of long-period events. The exact mechanism is unknown, but all of the suggested models involve fluid movement, which is usually the magma

propagation in the volcanic channel (Benediktsdóttir et al., 2022). Some tremors can have several sources and it is important to distinguish them from other non-volcanic sources based on the signal frequency range, strength, duration and variation in time (Eibl et al., 2015).

A clear sign of tremor presence on seismograms is a distinct signal of long duration spanning from minutes to weeks or even months (Fig. 3.1). This is the main distinguishable feature from earthquakes, which only last several seconds. Tremors can occur before and during eruptions, serving as one of the possible prediction methods (McNutt, 1992). While some tremors are continuous, others are less persistent and show a changing pattern of activity and quiescence (Benediktsdóttir et al., 2022).

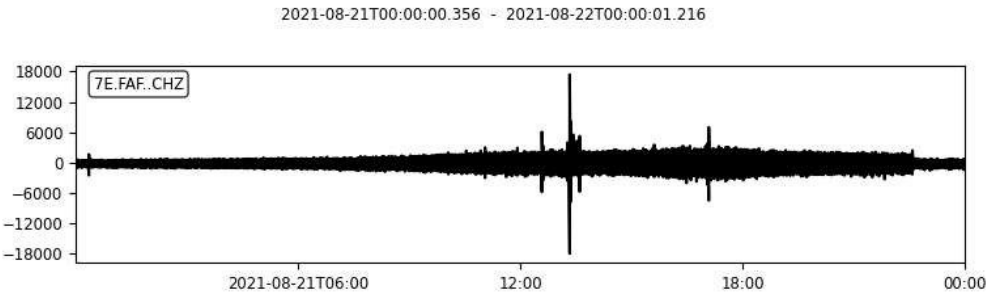

Figure 3.1: *Example of a volcanic tremor signature on a seismogram recorded on 21 August 2021 at Fagradalsfjall station. The main difference from an earthquake is the long signal duration.*

Tremors can propagate in the form of surface or body waves. Their frequency range is similar to the one of low frequency events, appearing between 1-9 Hz. This is different from most earthquakes, which have broader ranges including higher frequencies. According to observations gathered by McNutt (1992), tremors mean and median frequency is approximately 3.5 Hz. Their amplitudes are larger during more violent eruptions and in some cases the amplitudes can correlate with the heights of lava fountains (McNutt, 1992).

There are many studies documenting different kinds of tremors at different locations. The harmonic tremor has fundamental frequency shown as a peak in the spectrum with peaks at overtones and it was observed at Mt Semeru, Indonesia (Schlindwein et al., 1995) or Redoubt Volcano, Alaska (Hotovec et al., 2013). The monochromatic tremor with only one single narrow frequency band appeared on Mt Ruapehu, New Zealand (Hurst, 1992). Tremors with no distinct fundamental frequencies appeared on Hakone volcano, Japan. Their frequency spectrum consisted of a 1-6 Hz broad band, which was invariant with time and independent of amplitude (Yukutake et al., 2017). Also during the 2010 Eyjafjallajökull eruption, a tremor with frequencies up to 10 Hz was detected (Benediktsdóttir et al., 2022).

Computing the source location of volcanic tremors is complicated due to their emerging onsets, which hinder the determination of exact first arrival times (Eibl et al., 2015). Tremor sources have usually been localized in shallow depths, but some observations tracked them as far as 40 km in the subsurface (McNutt, 1992). Permana et al. (2022) located a tremor source beneath Sakurajima volcano directly in the conduit under the main crater and related the shallow tremor to ejection of gas and ash before explosive eruptions. During the 2010 Eyjafjallajökull activity, the detected tremor was located less than 1 km below the surface and consisted mainly of surface waves. It was stronger during the effusive eruptions than the explosive ones (Benediktsdóttir, 2022).

Non-volcanic tremors were detected around geysers during repetitive water eruptions (Kedar et al., 1996). Nayak et al. (2020) found the source of such hydrothermal tremor migrating between 4-20 m below the Lone Star Geysir, Yellowstone. The migration correlated with the stage of eruption, with the source moving upwards before eruption and downwards after the eruption reached its peak. The moment tensor was primarily made of the isotropic and compensated linear vector dipole parts (Nayak et al., 2020).

4 Site characteristics

4.1 Volcanism and tectonics of Reykjanes peninsula

Iceland is part of the mid-ocean ridge system between the Eurasian and North American plate, which are continuously drifting apart with a velocity of 1.9 cm per year. Despite the oceanic crust being generally very thin, a stationary magma plume located beneath the island causes its excessive thickening. Millions of years of dike intrusions and eruptions resulted in Iceland reaching 4 500 m above the surrounding seafloor (Blanck et al., 2019).

The Mid-Atlantic Ridge bends eastwards above the mantle plume, creating three major volcanic spreading zones on shore - North, East and West Volcanic Zone. Their rifting axes keep subparallel to the main ridge and their offset is connected with trans-tensional and fracture zones. While the fracture zones are non-volcanic, trans-tensional zones exhibit both transverse faulting and spreading accompanied by volcanic activity. The Reykjanes Peninsula in south-west Iceland is one of those trans-tensional zones, linking the West Volcanic Zone and submarine Reykjanes Ridge southwest of Iceland. The peninsula includes chains of NE-SW trending en echelon faults and fissures. It is formed by quaternary basaltic rocks from shield and fissure eruptions, with a clear age stratification. The youngest rocks can be found along the ridge axis with older rocks towards the edges (Saemundsson et al., 2020).

High seismic activity, volcanism and geothermal fields are typical for the area, creating clusters that can be separated into independent volcanic systems (Fig. 4.1). Taken from the west these are: Reykjanes, Svartsengi, Fagradalsfjall and Krýsuvík. Each of those systems has a central volcano and an area of high underground temperatures. From there, swarms of fissures are extending in NE and SW directions. The accumulated stress on the ridge is released in volcano-tectonic events including eruptions and microearthquake swarms on right-lateral strike-slip faults (Hrubcová et al., 2021; Saemundsson et al., 2020).

Before 2021, the last eruption on Reykjanes peninsula occurred in the 13^{th} century following the repeating pattern described by Saemundsson et al. (2020), where regular eruptions occurred once in 800-1000 years. The activity usually started in the east and shifted to the west, lasting several decades.

The earthquake swarms occurred more frequently than the eruptions, lasting several days, with some shocks reaching up to M_L 5-6 on the local magnitude scale. Their energy source was mapped to depths of 2-6 km in the subsurface, but deeper foci were also observed.

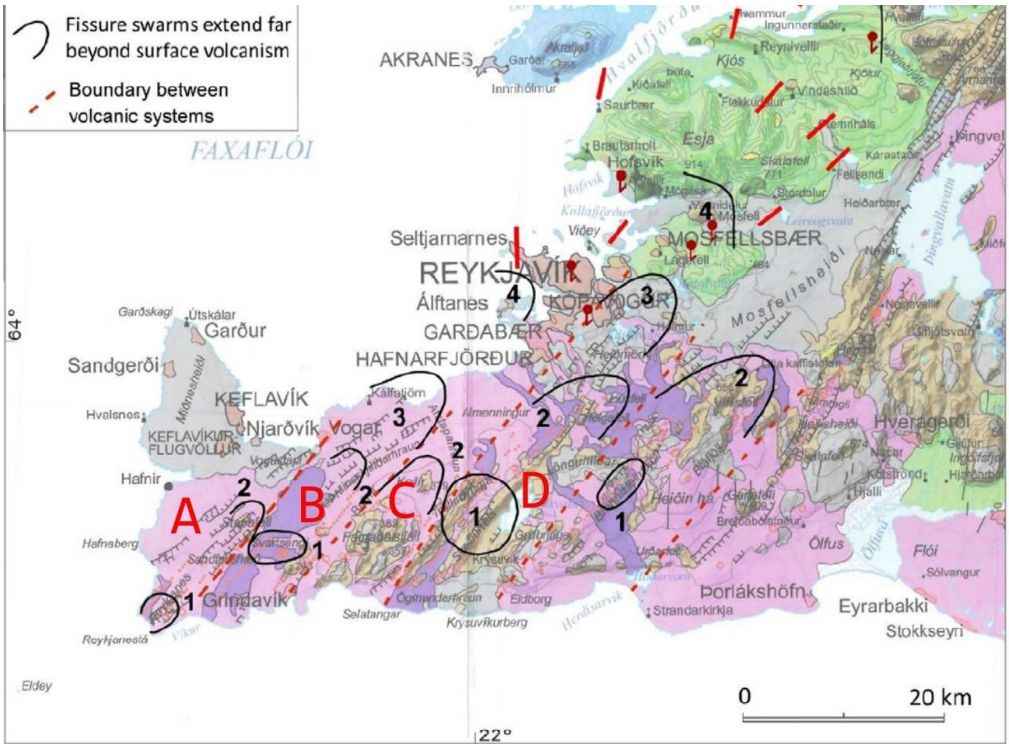

Figure 4.1: *Volcanic systems on the Reykjanes peninsula are NE-SW trending groups of fissures with a central volcano. They are positioned on the axis of Mid-Atlantic Ridge connecting the West Volcanic Zone in the east and submarine Reykjanes Ridge in the southwest. They include Reykjanes (A), Svartsengi (B), Fagradalsfjall (C) and Krýsuvík (D)(adapted from: Saemundsson, 2020).*

Despite most of the earthquakes are of tectonic origin, rising magma also contributes to the activity by filling freshly formed fissures and causing volumetric changes (Hrubcová et al., 2021).

4.2 Eruption at Fagradalsfjall

The Fagradalsfjall volcanic system is named after a tuya volcano located in its centre. The mountain is a result of a Pleistocene subglacial eruption and it has been dormant for several thousand years until 2021 (Global Volcanic Program, 2013).

There were many precursors before the eruption started on March 19, including increased seismic activity in the region. The earthquake swarms registered on Reykjanes Peninsula in the period between 2013-2019 were concentrated mainly within the Fagradalsfjall volcanic system. One swarm analysed in 2017 was aligned along WSW-ENE trending strike in depths between 2-6 km. The earthquake locations showed an aseismic gap in the middle, which

was contributed to a possible ductile magmatic intrusion in the place of future eruption (Hrubcová et al., 2021).

The seismic activity continued in the following years 2019-2020. Using seismic signals for tomographic imagery, Hobé et al. (2021) discovered a high v_p/v_s anomaly below the Reykjanes Peninsula. They interpreted it as a magma chamber in more than 10km depth, which was already visible in the data in May 2020. This finding stands in contrast with a previous study from 2014-15, in which Blanck et al. (2019) computed the v_p/v_s ratio from more than 2000 earthquakes in the area. At that time, they found no evidence of a shallow magma chamber in the crust under Reykjanes peninsula.

Hobé et al. (2021) discuss further, that the roof of the magma chamber was subsequently subjected to stress and its rupture was responsible for the strong earthquake swarm detected on 24 February 2021, few weeks before the eruption. As a result, a feeder dike propagated vertically upwards, but was stopped below the surface in 0.5-2km depth. Receiving constant magma inflow, it created 9km long regional dike towards NE. Another swarm occurred on March 14 and was connected to the dike propagation towards the surface with rate of 2 cm/s (Gudmundsson A. et al., 2021).

On March 19 at 20:30 UTC a fissure opened on the slope of the Fagradalsfjall mountain and lava began to fill the surrounding Geldingadalir valley. Initially there were 12 small vents along the 180m long fracture, but within few hours the activity was confined to Vents 1a and 1b (Fig. 4.2). The eruption was characterized by continuous bubble-bursting magma flow with occasional fountaining.
In the beginning of April other vents opened along the NE trending fissure. The last vents - Vent 5 and 6 appeared in the morning on 13 April. For the rest of the eruption Vent 5 remained the main centre of the activity, feeding the lava field through internal pathways and showing multiple periods of strong fountaining. Between 23 and 30 April the fountain heights were exponentially increasing, reaching a maximum of 250 m (Eibl et al., 2022).

Throughout May, lava discharge rate increased from 7 to 12 m^3/s, which is an unusual behaviour for volcanic systems fed from a shallow confined magma chamber. Therefore, the feeding channels were probably connected to a deeper magmatic source and the increased flow could be related to channel erosion (Gudmundsson M. T. et al., 2021).

On May 2, the so far continuous eruption suddenly changed into periodic pulsations. The process was characterized by bubbling magma rising to the surface, strong outgassing and lava fountains, which decreased towards the end of each period and time of inactivity followed. There were more than 7000 lava fountains between 2 May and 14 June (Eibl et al., 2022).

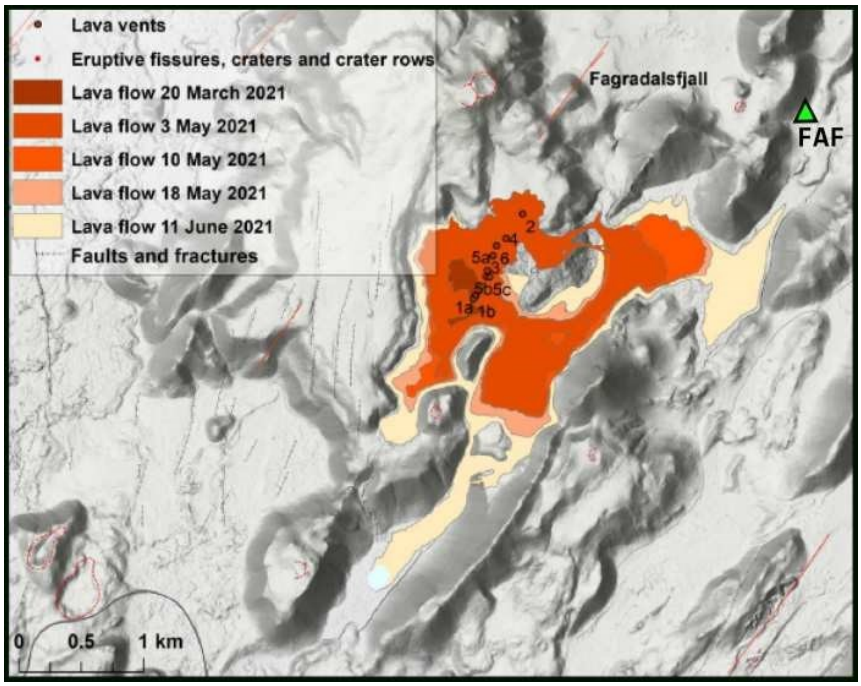

Figure 4.2: *Lava field extent of the Fagradalsfjall eruption and its development till 11 June. The closest seismic station FAF from the REYKJANET network is visible in NE. The topographic features often follow the NE-SW fissure direction. The lava vents are also oriented along similarly trending fissure (adapted from: Eibl, 2022).*

On 28 June the eruption entered a new phase, when it became inactive for several hours. Similar pattern of active/inactive windows continued till 2 September, when the eruption stopped. Multiple lava bursts occurred lasting from 12 to 24 hours and spaced with quiescence periods. During the still times, the crater was empty up to 70-m depth.

After several days of inactivity, the eruption resumed on 11 September, being active for another 7 days. After 18 September the volcano turned dormant, with a volcanic cone reaching 120 m above the former surface and the lava field covering more than 4.8 km^2 (Fig. 4.2; Gudmundsson M. T. et al., 2021).

During the following months, ground uplift was still measurable in the surrounding areas, suggesting ongoing crustal inflow. Also several earthquakes swarms hit Geldingadalir in December 2021 (Icelandic Met Office, 2021).

5 Methods and analysis

5.1 Seismic network REYKJANET

The data in this study come from a local seismic network REYKJANET on Reykjanes peninsula, which started recording in 2013 (Fig. 5.1). It operates under the Institute of Geophysics and the Institute of Rock Structure and Mechanics of the Czech Academy of Science. There are altogether 15 stations covering most of the peninsula's area (Fig. 5.2, left).

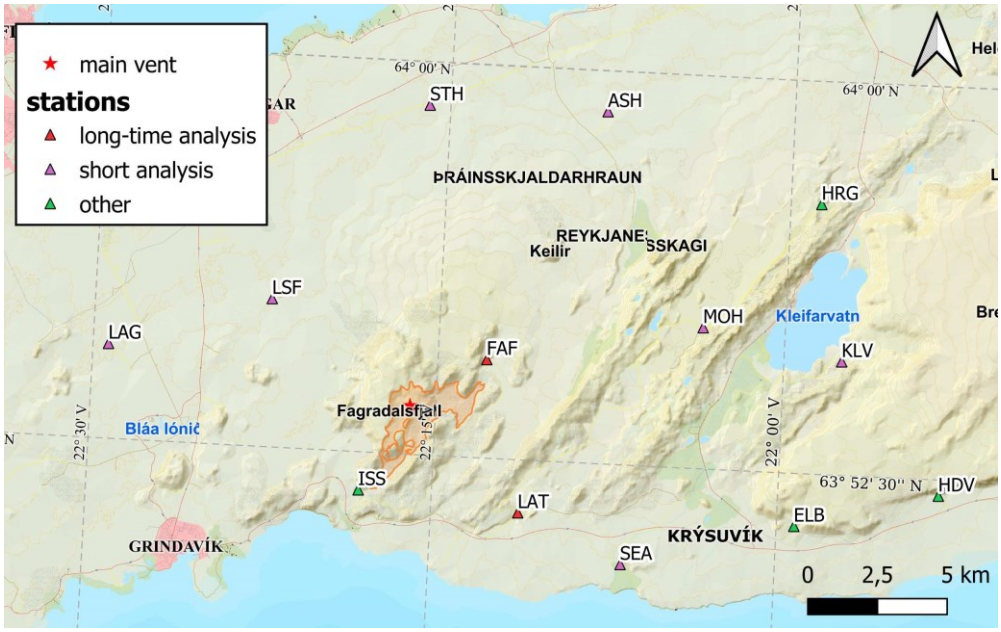

Figure 5.1: *Map showing the location of REYKJANET stations, surrounding the Fagradalsfjall mountain. The ISS station was not used in the analysis, because it was relocated during the eruption. The data from the two closest stations FAF and LAT were used for the reconstruction of half-year tremor activity.*

Former high-frequency seismometers were replaced by broadband Guralp CMG-3ESP seismometers (Fig. 5.2, right) with flat response of 0.03380 Hz (30 s - 80 Hz) and sampling frequency of 250 Hz. The sensors are 3-component, measuring ground velocity with gain of 400 V/m/s and the AD converter ratio 1.25 μm/count, resulting in the instrument response of 0.003125 μm/s per count.

The presented analysis used data from the following stations: Móhálsadalur (MOH), Látur (LAT) ,Fagradalsfjall (FAF), Stantharheidi (STH), Langahlíth (LHL), Littla Skógarfell (LSF), Afstapahraun (ASH), Selalda (SEA), Lágar (LAG) and

Kleifarvatn (KLV). Station Isolfsskali (ISS) could not be used, because it was endangered by the lava flow and later relocated (Fig. 5.1).

Figure 5.2: *One of the REYKJANET seismic stations Littla Skógarfell (LSF) and the type of used seismometer - Guralp CMG-3ESP (source: Geofyzikální ústav Akademie věd ČR, v.v.i (online); CMG-3ESP Operator's Guide, 2016).*

5.2 Preliminary analysis

Most of the data analysis in this study was done in Python, more specifically in its Integrated Development Environment (IDE) PyCharm. Python was chosen, because it is an open-source high-level programming language, which has a large community and it can be effectively used in any scientific analysis. It has many libraries, ranging from general tools like *NumPy*, used for array operations, to more specific ones, like *ObsPy* for handling seismic data. For graphical outputs, the *Matplotlib* library was used, which is equivalent in its methods and design to MATLAB.

The miniSEED files from REYKJANET were separated based on the station name, channel and day. The first step of the analysis was the creation of a script, that would automatically load data from a specific station, channel and day into Stream and remove the mean using detrend.

For the preliminary tremor detection, only the vertical component (CHZ channel) of the closest station Fagradalsfjall (FAF) was chosen. The Icelandic Met Office regularly published real-time data on their website, which showed an

indication of a tremor activity in late August and early September. Power spectral density (PSD) was computed and plotted on a spectrogram for several days in this period to find the tremor's frequency range (Fig. 5.3).

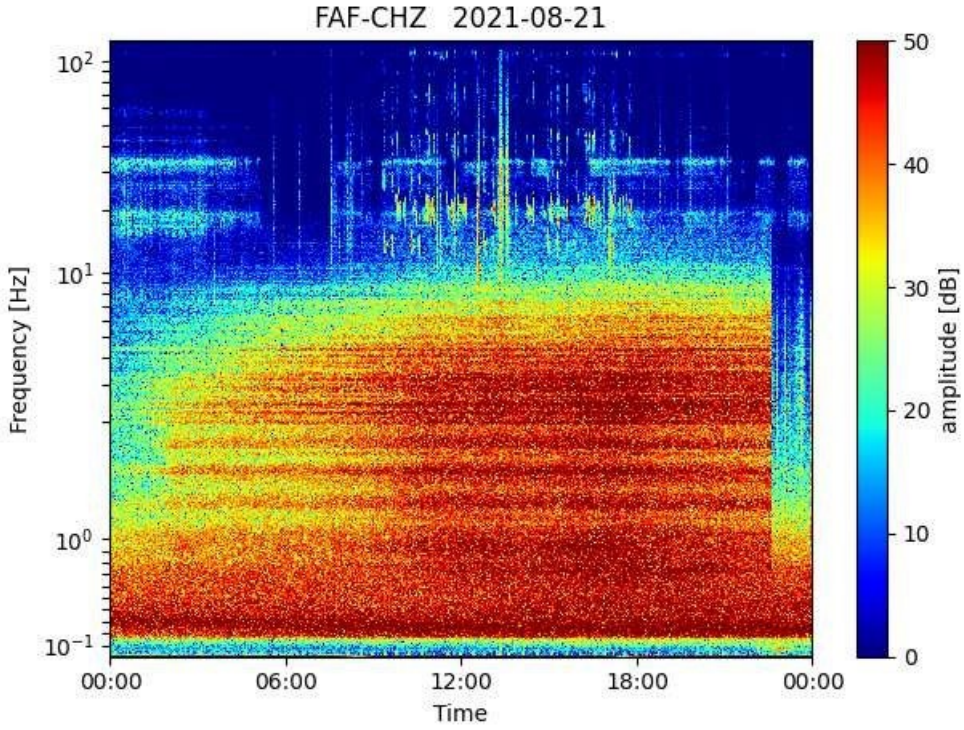

Figure 5.3: *PSD spectrogram of signal from FAF station on 21 August. The observed tremor frequency range of 1-10 Hz determined the filtration passband in the preliminary analysis.*

The PSD was computed using Fast Fourier Transform (FFT) and moving Hanning window with a size of 100 000 points (equivalent to 400 s) and a step of 50 000 points. In the spectrogram, there was a strong indication of a tremor occurrence in the frequency range between 1-10 Hz, therefore it was chosen as the passband for applying a notch Butterworth filter.

After the filtration, the next processing step was to emphasize the tremor signal on the plots and also to decrease the sampling rate of the trace.
Considering the time and memory constraints of processing the half-year signal, most of the data points were omitted. In order to improve the signal-to-noise ratio in the plots, several methods were applied (Fig. 5.4).

First the waveform amplitude envelope was computed using the Hilbert transform, which shifts the phase spectrum of signal by $\pi/2$ without changing its frequency content (Shearer, 2009). The amplitude envelope reflects the maximum potential amplitude at any given moment and shifts the signal into positive values.

After the computation and plotting, it showed very oscillating signal (Fig. 5.4 and Fig. 5.5). Furthermore, it reinforced the signal of low-frequency earthquakes, which have short duration, but several times greater amplitudes than the tremor. Those events were considered as noise in the tremor signal. Additionally, the Hilbert transform was slower to compute as it worked with the original data size (in this case decimation would produce unwanted distortion and information loss).

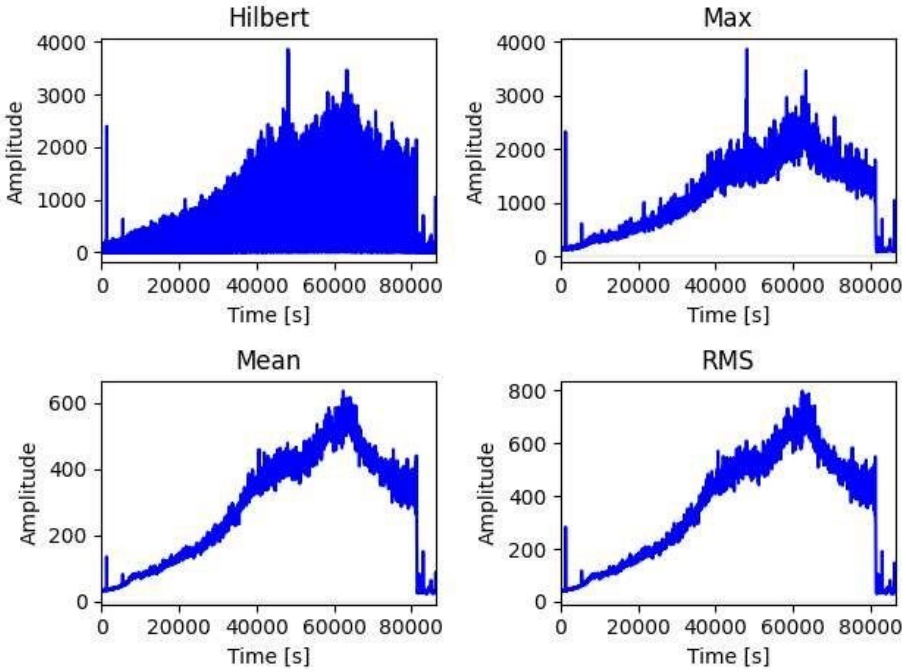

Figure 5.4: *The preliminary analysis sought the improvement of tremor signal in relation to the noise and earthquake signal. A reasonably sized window of 10 000 points (40 s) with no overlap was chosen for the Max, Mean and RMS amplitude computation. The amplitude envelope (Hilbert) and maximum amplitude (Max) were oscillatory and did not suppress the earthquake signal. The mean and RMS amplitudes showed better results.*

Also, other tremor enhancement methods were tested, including the maximum amplitude, mean amplitude and root mean square (RMS). All of them were computed in a window of certain length and step, which substituted the decimation process (Fig. 5.4).

Maximum amplitude was keeping only the maximum value in the window. It reduced the signal oscillations, but similarly to the amplitude envelope it preserved all of the high magnitude earthquakes. Despite the mean and RMS methods decreased the absolute value of tremor amplitudes, the signal-to-noise ratio was

improved. After plotting, both showed similar results, with less oscillations. The RMS amplitude was chosen for the analysis.

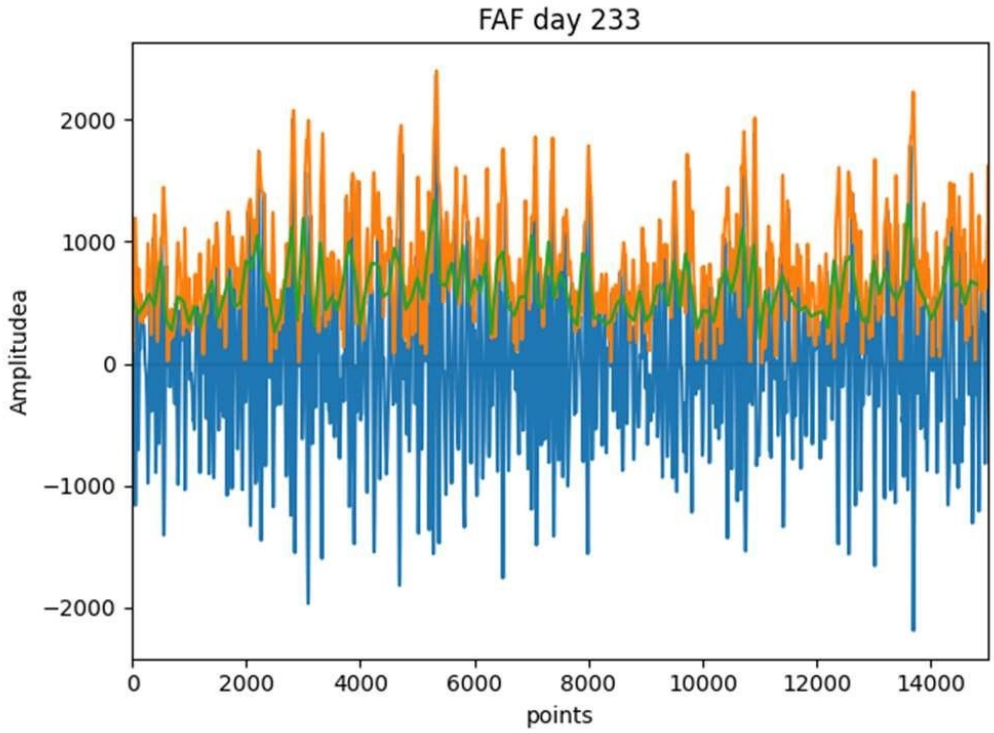

Figure 5.5: *Comparison of the amplitude envelope (orange) and root mean square (RMS) amplitude (green) computed from the seismic signal (blue). The amplitude envelope showed more oscillating curve than the RMS.*

Parameters of the RMS amplitude computation included the window length and the decimation factor. Generally, the decimation in signal processing increases the sampling interval and it is the contrary of interpolation.

Originally the data were sampled with 250 Hz, which resulted in over 21 million data points per day. Because the analysis was focused on events lasting from minutes to days, the new sampling step was chosen to be 120 s, which corresponded to a 30 000-point window. One day consisted of 720 data points, substantially reducing the sample size and shortening the processing time. Considering the Nyquist frequency, it was enough to distinguish tremors of duration longer than 4 minutes, which was considered a sufficient resolution.

The tremor signal was also compared in between stations and individual days before the filtration and decimation. The amplitude spectra of a short 10-min segment with a clear tremor appearance were computed using the FFT. First for

the closest FAF station and then also for the LAT and MOH stations. A 10-min segment with no tremor signal was added as the noise reference. The results were very oscillatory, therefore they were smoothed using the Savitzky-Golay filter. This filter is an equivalent of low pass filter derived for spectral analysis. It computes the polynomial weighted moving average, which reduces the noise but preserves the original shape and height of peaks (Schafer, 2011). The window size of 251 points (approximately 1 s) and 4^{th} order polynomial showed good results.

The preliminary analysis concluded that for plotting the long time tremor series, the following procedure can be applied: bandpass filtration between 1-10 Hz and RMS amplitude computation in 120s long windows with no overlap.

5.3 Long time series

Producing the long-time waveform involved joining Traces from several days together. One of the challenges were data gaps, which were caused by station outages and failed uploads to the server. The gaps were usually in the scope of hours per day, but sometimes data from a several-day period were missing. For each of those days, an artificial Trace was generated, including necessary stats and a data array with values set to 0.0. The day gaps were easier to handle with help of the *ObsPy* toolbox. Using the trim method, Traces were padded to the specific UTC time and filled with 0.0 values. Subsequently the first Trace was enlarged by the following ones using the __add__ method.

The long array was then filtered and decimated using the procedure suggested in the preliminary analysis (Section 5.2). Except the FAF station, all of the other stations were filtered using a different bandpass between 1-5 Hz, which was visually determined from their PSDs. The resulting amplitude vector consisted of data from 180 days spanning from 11 March to 6 September and was exported into a separate .txt file for easier manipulation.

Apart from the visual interpretation, several other methods were applied on the obtained long-time series. This part of analysis did not involve manipulation with large data sets and was done in MATLAB.

To quantify the resemblance of traces between stations, a cross correlation was computed using an adapted script. It used a moving Tukey window of size 50 (equal to 100 min). Tukey window is a tapered cosine window with a specific taper fraction. Window with a taper fraction 0 is equivalent to a rectangular window and window with a fraction 1 is the Hanning window.

To assess the periodicity of reoccurring tremor pulses, a PSD was computed from the pseudosignal of RMS amplitudes. The FAF station was chosen in this analysis for its strongest signal. The basic unit of time was a day, resulting in frequency of events per day. The sampling frequency remained the same as in the time series.

5.4 Noise influence to tremor amplitudes

To assess the influence of noise on the tremor amplitudes further away from the source, a representative day with a complete tremor was chosen. Then the signal was processed using the methods described in Section 5.2 to obtain the RMS amplitudes. The amplitudes at the closest FAF station were then compared to the LAT station and plotted in the same graph (Fig. 5.6). The amplitude ratio was then computed in every point of the series and also plotted.

The amplitude ratios were relatively constant only when the tremor signal was strong. In the beginning of the day, during the slow tremor onset, the ratio was gradually increasing. It started from the value of 1.0, representing similar noise levels on both stations and during the next 6 hours it reached a plateau of relatively constant amplitude ratios.

The long rise seemed to be an artifact of a small signal-to-noise ratio (SNR) at distant stations, when the source signal was not strong enough. A simple model was computed (Fig. 5.7), following the equation

$$\frac{A_{t1}}{A_{t2}} = \frac{\frac{A_0}{r_1} + A_N}{\frac{A_0}{r_2} + A_N}.$$

It assumed only the geometrical spreading factor of $1/r$ to be part of the attenuation. The noise amplitude A_N was set to a constant and the amplitude ratios A_{t1}/A_{t2} were computed for different source amplitudes A_0 and different distance ratios r_2/r_1. Supposing the source of the tremor around the eruption vents, the LAT/FAF ratio was 1.75, and the MOH/FAF was 3.5.

The model confirmed the theory. When the source tremor amplitude A_0 is not high enough in comparison to the noise A_N, the amplitude ratio gets distorted. For low A_0 it approaches the ratio for noise, which is the same at all stations and therefore it was set to 1.0. At distant stations, where the source amplitudes are attenuated, the ratio gets distorted more easily and is underestimated. This explains the gradual rise of the ratios computed from the RMS amplitudes, despite the modelled curve has a slightly different shape. The model only accounts for the decrease of amplitudes with distance due to geometrical spreading, but the real data are affected also by other sources of attenuation.

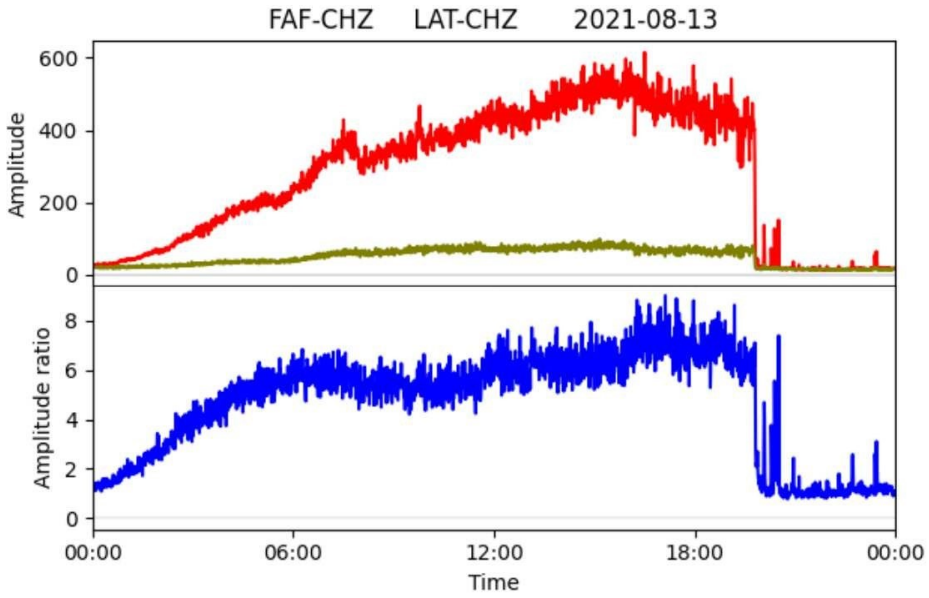

Figure 5.6: *Comparison of RMS amplitudes at FAF and LAT stations on 13 August (top). Their amplitude ratio is approximately 6.0 (bottom). Before the tremor reaches higher amplitudes, the ratio is not constant - between 00:00 and 6:00 at both stations.*

5.5 Amplitude attenuation analysis

For estimating the amplitude attenuation between stations, a bigger sample of 9 stations from 21 August was used for comparison. The RMS amplitude series from that day contained a day-lasting tremor, but also a part with no tremor activity. They were all plotted into one graph to compare the tremor amplitudes. To account for the base noise differences, the SNR ratio was computed for all stations. In this case the term signal and noise are referring to the tremor and noise RMS amplitudes. Both were computed from 110 points in a representative 73-min long window.

The amplitude-distance graph showing the amplitude attenuation was plotted, assuming the source location at the surface near the main vents. To find the relationship describing the change of amplitude A with increasing distance r from the source, the following equation was applied:

$$A(r) = A_0 \left(\frac{r_0}{r}\right) e^{\alpha(r_0 - r)}$$

It constitutes of both the geometrical spreading factor $1/r$ and the anelastic attenuation, described by the exponential part e^x. The A_0 and r_0 are the amplitude and the source distance of the reference station.

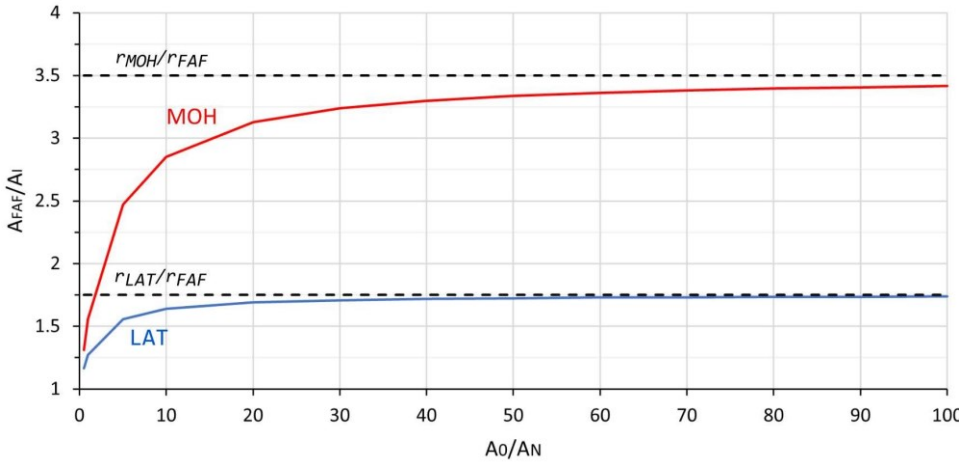

Figure 5.7: *Amplitude ratio is distorted based on the source signal amplitude A_0 and the noise amplitude A_N (same in all places, set to 1). The two dashed lines are representing different station distance ratios. The amplitude ratios FAF/MOH (red) and FAF/LAT (blue) are approaching the value of distance ratios for high A_0, but for low A_0 are underestimated. The model takes into account only the amplitude attenuation caused by geometrical spreading* ($1/r$).

After choosing the FAF station as a reference, an inverse problem was computed using a discrete range of attenuation coefficients α. It used the data from all stations to find the best α, which would result in a minimum residual between the computed and measured amplitudes. The L2 and L1 norms in a form

$$\epsilon = \sum_{i=1}^{n} (A_r - A_i)^2 \qquad and \qquad \epsilon = \sum_{i=1}^{n} [A_r - A_i],$$

were used, to compute the size of the residual. A_r was the amplitude at the FAF reference station and $n = 8$ was the number of stations. The coefficient α was supposed to be uniform in the subsurface, which does not reflect the complex reality. Therefore, different reference stations were also used to compare the results, alongside with a logarithmic variant of the L1 norm.

6 Results

6.1 Tremor description

Already the preliminary analysis of data from the FAF station confirmed the presence of a distinct tremor activity during the eruption. While the background noise was constant on different days and between stations, the signal in higher frequencies showed some temporal changes.

PSD spectrograms of seismic signal from the LAT and FAF stations on 21 August showed a long duration event with a visible change of frequency content (Fig. 6.1). It emerged from the seismic noise at approximately 1.0 Hz and over time it gradually included all frequencies spanning up to 10.0 Hz. The strength of this signal was weaker on the LAT station, which is further from the eruption, but the frequency content was comparable. While the onset of this event lasted a couple of hours, the end was abrupt and confined into several seconds. This pattern was typical for all long-lasting events in the investigated period. After taking the time duration, frequency content and location into account, the seismic signals were classified as a reoccurring volcanic tremor.

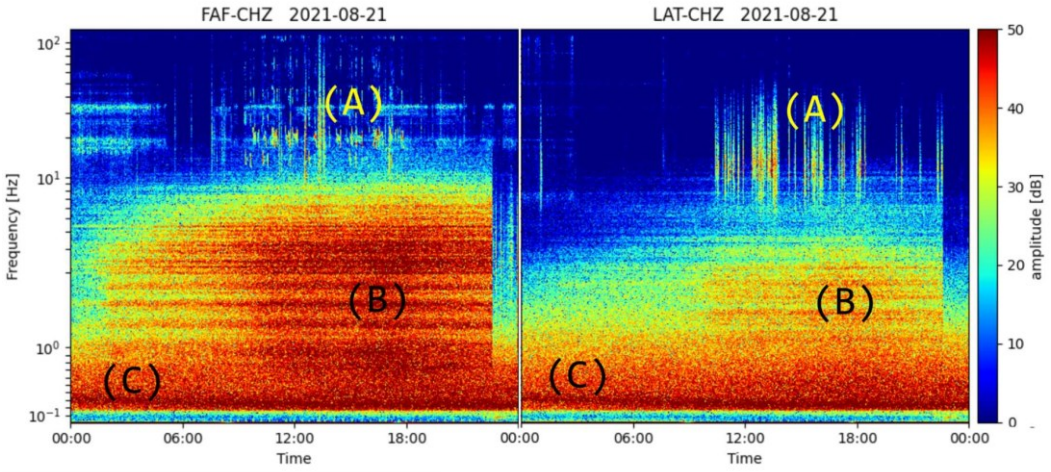

Figure 6.1: *PSD seismograms from FAF (left) and LAT stations (right) on 21 August, showing the frequency content and time duration of earthquake swarms (A), volcanic tremor (B) and omnipresent noise (C), which includes microseismic peak around 0.2 Hz (logarithmic scale).*

The tremor was distinguishable from other events, including earthquake swarms, which appeared to have a shorter duration and, more importantly, a different frequency range. At the FAF station on 21 August this range was visible

between 10-100 Hz, while at the LAT station it was between 8-40 Hz. The observed noise frequencies were concentrated below 2.0 Hz with a strong frequency band around 0.2 Hz, equivalent to 5 s. This band was omnipresent at all stations and it falls into the frequency range of microseisms.

The tremor signal strength varied between stations. Further from the eruption vents the tremor was weaker as the high-frequency components were attenuated. The same pattern was also observed in earthquake signals. Both agree with Earth acting as a low pass filter.

For comparison, the computed magnitude spectra (Fig. 6.2) from 23 July and 13 August, when equivalent day-lasting tremor occurred, provided similar results to the PSD spectrograms from 21 August. The spectra included a representative tremor sample from the LAT, MOH and FAF stations together with a representative noise sample from the FAF station.

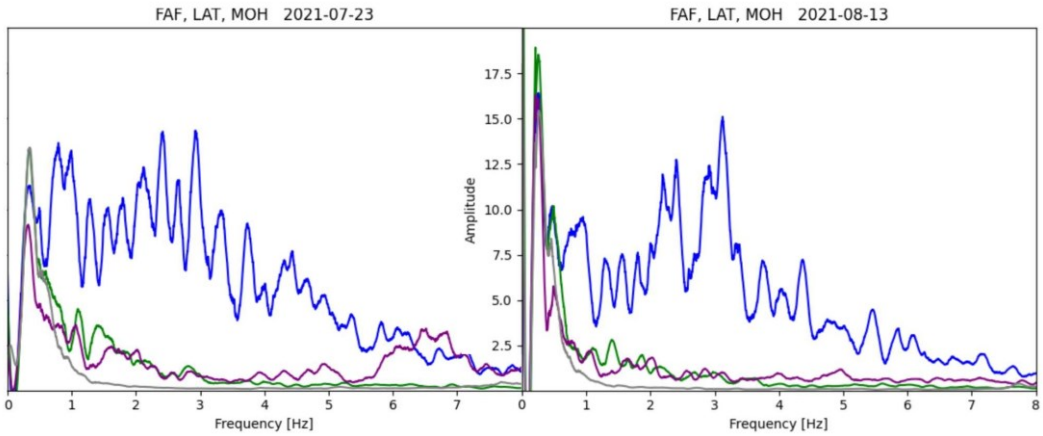

Figure 6.2: *Magnitude spectra of two short time segment from 23 July and 13 August, during a tremor occurrence. Frequency content of the signal at the FAF (blue), LAT (green) and MOH (purple) station is shown, together with a noise frequency content from the FAF station (grey). The tremor spectra are similar between the days and there is a common microseismic peak around 0.2 Hz.*

When comparing spectra between the two days, the tremor and noise frequency contents were similar at all three stations. The exception was the microseismic noise, which was stronger on 13 August (Fig. 6.2, right), when it exceeded even the tremor signal. The noise frequencies did not change with time, showing one dominant peak around 0.3 Hz and one minor peak around 0.5 Hz. The noise magnitude decreased substantially in frequencies over 1.0 Hz.

Another major difference between the day spectra was the increased frequency content around 6.5 Hz at the MOH station on 23 July, which was attributed to a different low-frequency event.

On both days the tremor spectra at the FAF station ranged from around 0.7 Hz to more than 8.0 Hz and it contained no major peaks. Instead, it consisted of a row of several minor peaks with varying magnitudes, even after the smoothing. The most prominent peaks were detected around 0.9 Hz, 2.4 Hz and 3.0 Hz. The spectra of the LAT station had lower magnitude and its range spanned from 0.7 Hz to approximately 4.0 Hz on both days. The few visible peaks were around 1.1 Hz and 1.4 Hz and did not match with those in the FAF spectrum.

The MOH station had a spectrum similar to the LAT station, with the same 1.1 Hz peak and one other at 2.0 Hz. At the MOH station, unlike at the other stations, the signal magnitude did not significantly decrease in the higher frequencies. This might be a result of a different noise level at the MOH station in comparison to the plotted noise measured at the FAF station.

Surprisingly, both the LAT and MOH stations showed similarly attenuated signal, despite the MOH station being in double distance from the eruption site.

6.2 Long time series

From one-day windows it would be difficult to describe any potential long-term pattern or changes of the tremor characteristics. Therefore, the whole eruption time was investigated using the RMS amplitude series from the closest FAF and LAT stations.

Despite several data gaps in both series, the RMS amplitudes resembled each other over the entire period (Appendix A). Apart from periods with long lasting tremor, there were also highly oscillating parts, which were difficult to visually compare in the plots. The computed cross correlation between the series was strong during those periods, which confirmed the tremor presence and ruled out any random process. The signal at the LAT station was permanently lower than at the FAF station, with a constant ratio of approximately 1/6.

There was a clear onset of a continuous tremor at the FAF station on 19 March (Fig. 6.3). The LAT station had a short data gap in that time. The start of the tremor around 21:00 matched with the documented beginning of the eruption. The PSD spectrogram of that day showed several earthquakes prior to the tremor onset. Most of them had a broader frequency range than the tremor, reaching up to 20 Hz and more.

It was important to differentiate between those signals when drawing conclusions from the filtered RMS amplitude series, where low frequency earthquakes and short volcanic tremors had similar signatures.

After the onset on 19 March, the tremor was continuous for several weeks till 2 May. The RMS amplitude slightly decreased on 28 March, denoting very low tremor activity lasting several days. After that, there was a slow increase and decrease of amplitudes, but they remained relatively low in comparison to the

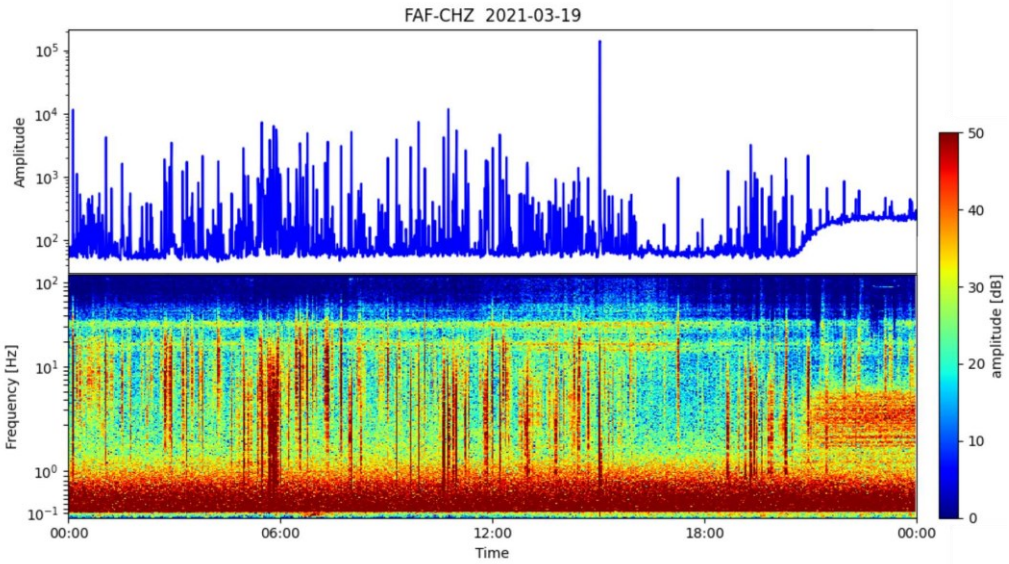

Figure 6.3: *Beginning of the eruption at the FAF station on March 19. There is an emerging tremor onset around 21:00, visible both in the RMS amplitude series (top) and in the spectrogram (bottom). Low frequency earthquake swarms are common prior to the tremor onset.*

following period beginning on 2 May. Earthquakes continued to appear, but not as frequently as in the period before the eruption.

On 2 May the continuous tremor ended after 43 days. A new pattern of activity began in the form of short time tremor pulses (Appendix A). On the first day, the pulses got gradually shorter and more frequent without a major change in their amplitudes (Fig. 6.4). In the following days their amplitudes started to grow and they continued growing till 10 June despite two clear setbacks. This period of short pulsations lasted 40 days and towards its end it showed one of the strongest pulses (Appendix A).

In the days following 10 June, the RMS amplitudes did not show any distinct pattern. The tremor pulsations remained, but with a fluctuating amplitude and irregular occurrence. There were no data available at the LAT station during this period, which could be used for the cross-correlation analysis.

On 14 June, the continuous tremor returned, but with higher RMS amplitudes than the one in the beginning of the eruption. The earthquake activity was sparser during this period and the RMS amplitude slightly increased over time. After more than 10 days, the amplitude started to slowly fluctuate and several short time pulsations occurred. On 28 June, the tremor activity sharply increased and then completely stopped for several hours, for the first time since the onset on 19 March. It resumed in the early hours of the next day and lasted additional three

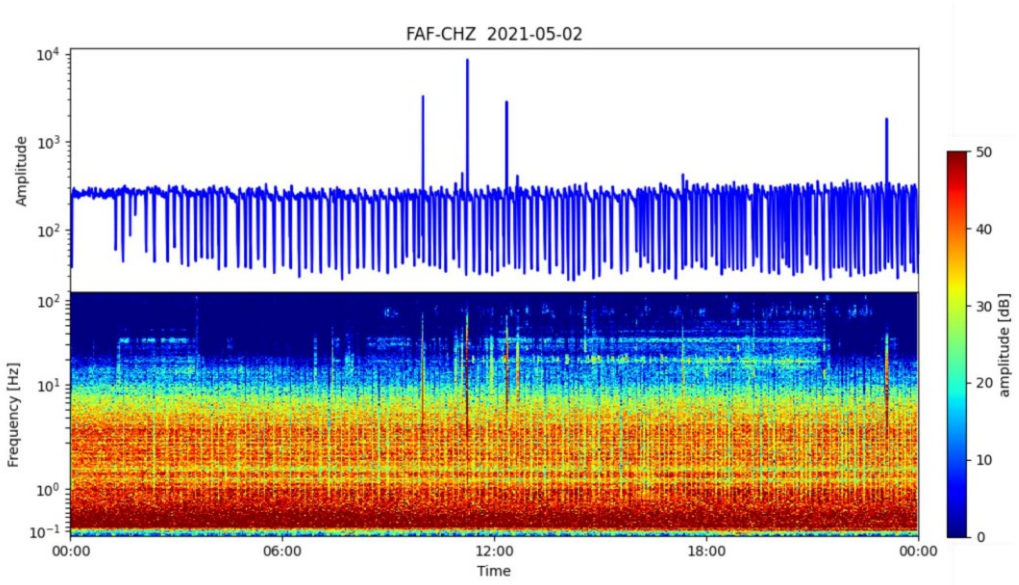

Figure 6.4: *Beginning of the tremor pulsations on early 2 May at the FAF station. The frequency content and RMS amplitude of the tremor remained unchanged throughout the day, but its pulsations were gradually shortening and becoming more frequent.*

days, before it stopped again. This time period showed no prevailing pattern. The tremor was continuous with varying amplitude and a period of short time pulsations. The end of the activity was similar to the previous one, preceded by a sharp amplitude rise and a couple of strong short pulses (Appendix A).

In the period between 2 and 6 July two long period tremors occurred. They both lasted more than a day and showed similar amplitude characteristics (Fig. 6.5). Despite the signal being strong on both stations, there was no clear correlation. This was due to the short window length, which reflected all small oscillations in the signal into the cross correlation. Those small oscillations can be regarded as noise, therefore the correlation coefficient varied. The only exception were the onsets and endings of both tremors, where the correlation coefficient was close to 1.

The following period from 7 July was characterized by an intermittent tremor activity. These tremors had emerging onsets, but after several hours of continuous signal they transitioned into pulsations (Fig. 6.6). Some of the pulses seemed to have the same emerging onsets and sharp endings like the long lasting tremors. The longest period of pulsations occurred between 10 and 14 July and showed unusually high and stable RMS amplitudes.

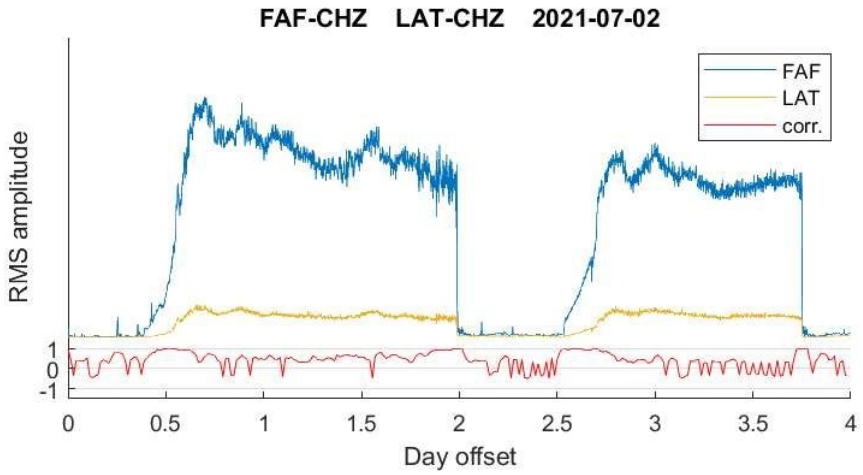

Figure 6.5: *Two tremors at the FAF and LAT stations, which occurred between 2 and 6 July showed similar amplitude characteristics, but no strong correlation. The correlation coefficient is close to 1 only in the time of onsets and endings of the tremors.*

On 20 July the activity pattern became more regular again. Approximately day lasting tremors started to regularly appear, spaced with shorter windows of inactivity in between. There were altogether 30 tremors in a row in the month and a half period. After 7 August their shape and amplitude got highly regular, resulting in a teeth-like pattern on the time series plot (Appendix A). The maximum RMS amplitude usually appeared in the middle of the tremor, signalling a reversal of the activity.

The final day-lasting tremor ended on 2 September and there was a period of quiescence for several days. A semi-continuous tremor reappeared later between 11 and 18 September. It shifted into a pulsating activity after the first two days. This was a very similar behaviour to the tremors, which appeared in mid-July. This time the tremor activity terminated and did not resume.

During the eruption there were three main tremor activity patterns: (i) First one was the continuous tremor, which appeared mainly in the very beginning of the eruption and had low amplitudes. It was also observed in the second half of June. (ii) Second pattern was the short time pulses, prevailing in May and the beginning of June. They were also part of the signal on several other days. Their amplitudes and characteristics varied, but they were indicated by a strong cross correlation between the stations. (iii) The last pattern was the long time pulses, marking the final part of the eruption. Most of them had relatively high amplitudes and were separated by periods of quiescence.

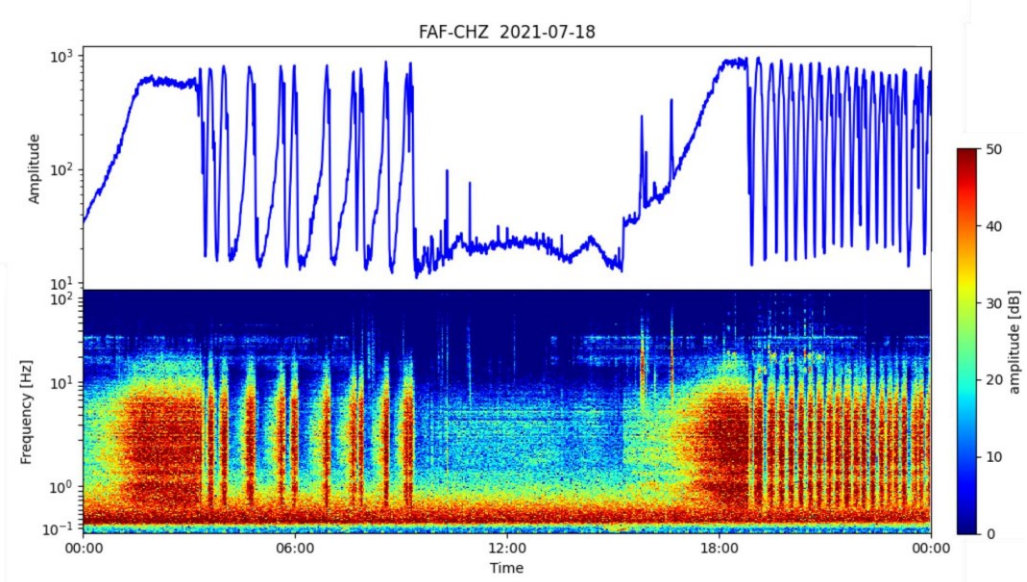

Figure 6.6: *Spectrogram and RMS amplitude of tremor activity on 18 July at the FAF station. Mid July was characterized by continuous tremors transitioning into pulsations. Some of the short pulses showed the same emerging onsets and sharp endings as the long lasting tremors.*

6.3 Tremor pulsations

The periods of short time pulses were analysed in more detail to understand their characteristics. The PSD spectrograms showed reoccurring and regular tremors with a higher frequency content, reaching up to 20 Hz (Fig. 6.7).
This is in a relation with a higher amplitude (energy) of the short-time tremors observed on several days.

Some pulsations were more irregular, while others contained equidistantly spaced pulses with repose times in between. The repose times seemed not to correlate with the duration of the individual pulses. The shapes of the pulses were not uniform and only few had the emerging onsets observed in longer tremors. There were pulse periods with both gradual onsets and endings as well as periods with sharp edges.

To estimate the changes in periodicity, respective in the length of the short tremor pulses, spectrograms were computed from the pseudosignal of RMS amplitudes (Fig. 6.8). Due to the chosen sampling rate of 720 points per day, the maximum frequency was limited to 360 events per day.

In the beginning of the pulsation on 2 May, there was no prevailing frequency, but after the first day the pulses started to appear more regularly with the frequency of 180 events per day. The frequency then slowly decreased to around 130 events per day, while the RMS amplitude gradually increased. The pulse

length was between 8 - 11 minutes, including the repose time. In the following days in May, the shortest regular pulses had approximately 6 minutes period. The longest pulses lasted around 14 minutes.

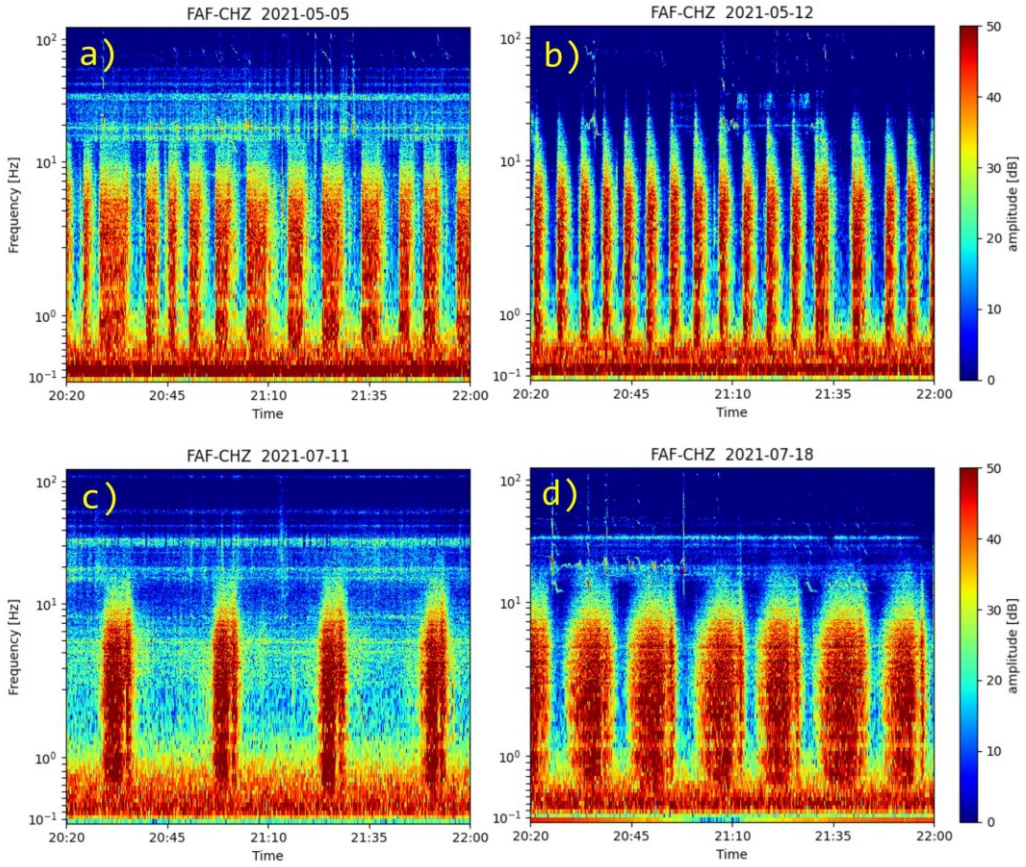

Figure 6.7: *Short time tremor pulses recorded at the FAF station had different characteristics throughout the eruption. The repose time did not match with the pulse duration. The pulses were irregular and with sharp edges on 5 May (a), regularly spaced and with higher frequency content up to 20 Hz on 12 May (b), composed of two consecutive pulses in July, with gradual onsets and endings (c, d).*

In July, when similar pulsations appeared, the pulses were generally longer, reaching to periods around 25 minutes (Fig. 6.9). The pulsations had high amplitudes and emerged from continuous tremors. Some of them started with the initial frequency of 60 events per day and then increased to 120 events per day. This clear shift was visible on the spectrogram on 10 and 18 July.

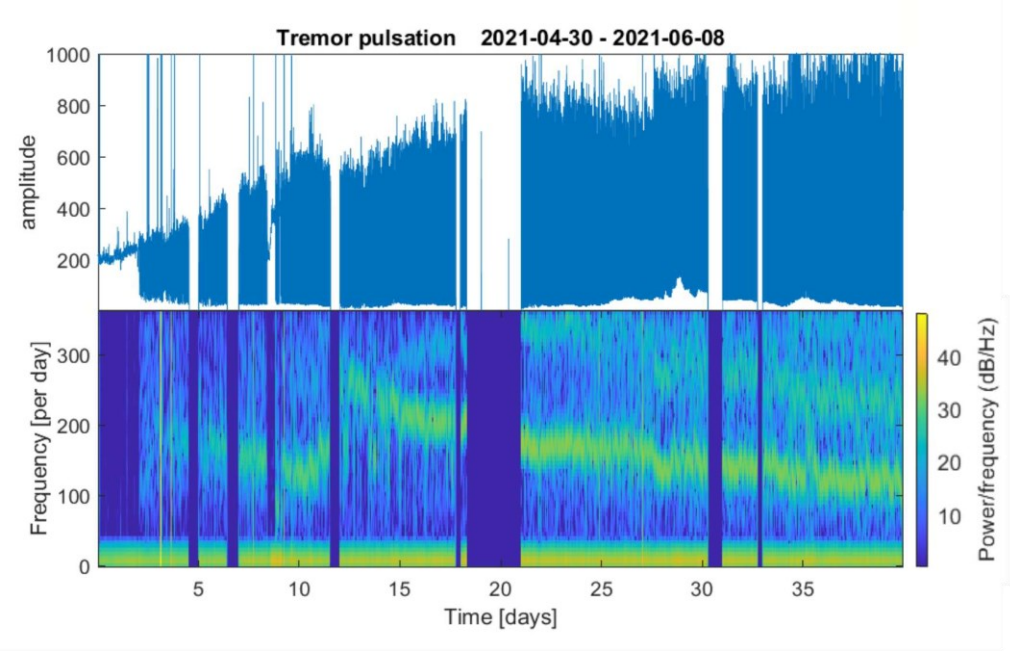

Figure 6.8: *Tremor pulsation spectrum (bottom) computed from the pseudosignal of RMS amplitudes (top) at the FAF station, starting on 30 April and covering the following 40 days. The period of pulses changes, spanning from 130 up to 240 events per day (6-14 min). The plots show an inverse relation between the pulsation frequency and the tremor amplitude.*

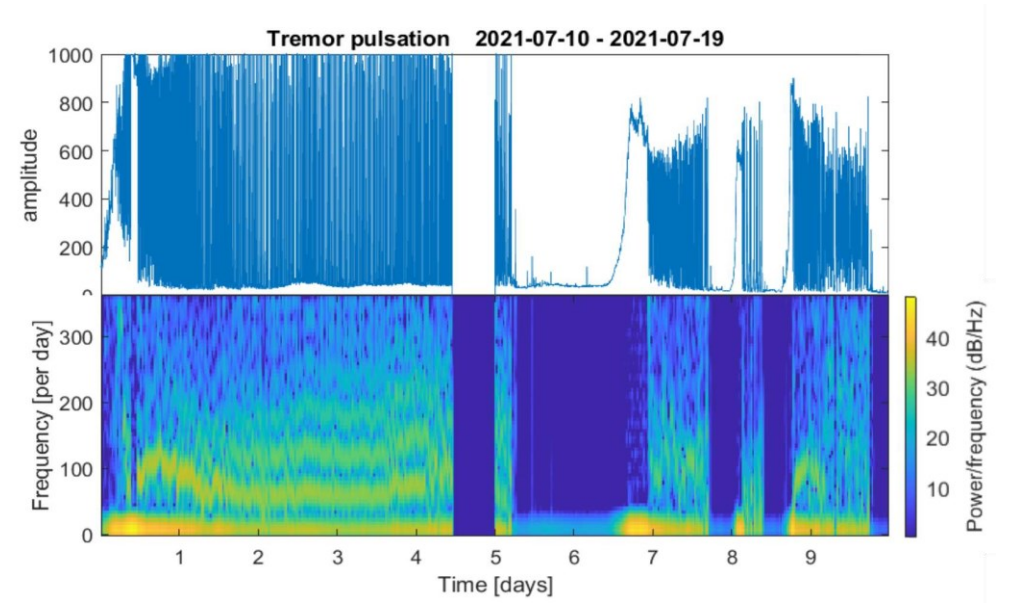

Figure 6.9: *Tremor pulsation spectrum at the FAF station between 10-19 July. The pulsations on the first and last day start with a clear frequency shift from 60 to 120 events per day.*

The periodicity of the long-time pulses was estimated from the amplitude time series (Appendix A). Between 20 July and 2 September, there were in total 30 tremor events, with very similar characteristics. Their period was estimated to be approximately 1.5 days. The repose time between them was slightly shorter than their duration.

6.4 Tremor attenuation between stations

In the long time series, the comparison between the LAT and FAF station showed a substantial attenuation of amplitude with distance. Using the RMS amplitudes from 13 August, the tremor signal was estimated to be approximately 6.0x stronger at the FAF station. Repeating the process with the RMS amplitudes from the MOH station on the same day, the signal at the FAF station was 7.5x stronger.

For better assessment of the tremor attenuation with distance, the RMS amplitudes from 9 stations on 21 August were used (Fig. 6.10). The tremor signal at the FAF station was exceptionally strong, not only in comparison to the LAT station, but also in comparison to the other stations. Another strong signal was detected at the SEA station, which is 9.4 km from the vents. It is in the same direction as the closer LAT station, which showed lower tremor amplitude.

The noise level varied a lot between locations. At some stations the

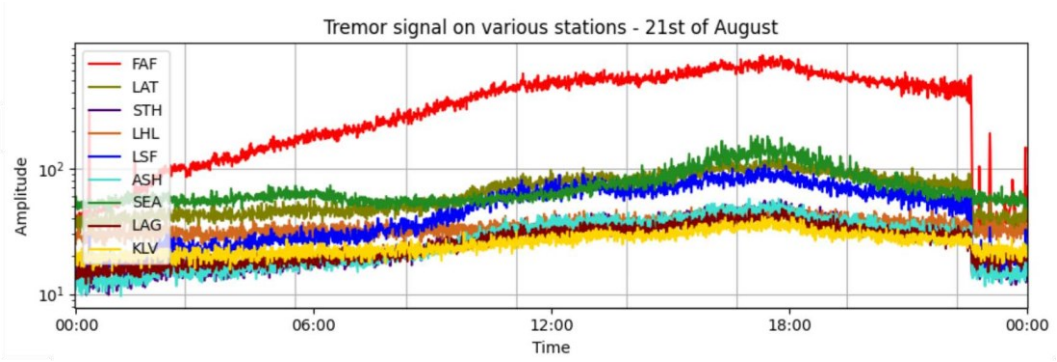

Figure 6.10: *RMS amplitudes showing a day-long tremor at 9 stations on 21 August. There is a difference in noise levels between the stations (visible between 23:00 - 00:00). The tremor is detectable also at the furthest LHL station (orange), which has the smallest SNR ratio.*

recorded noise amplitude was 4x higher than at others. High values were detected especially at the two stations closest to the southern coast - LAT and SEA, where the wind and sea were contributing to the noise. The high noise levels at FAF, LAT, SEA and LHL stations seemed to increase their tremor amplitudes. To account for that effect, SNR ratios were computed from a representative tremor and tremor-free time segments.

The highest SNR ratio of 17.46 was at the FAF station, while it did not exceed 5.0 at distant far stations (Table 6.1). The lowest SNR ratio was 1.35 at the furthest station LHL, which is 23.5 km away from the eruption vents. That proved that the tremor was detectable even in great distances.

Table 6.1: *9 stations analysed on 21 August and their distances r, tremor amplitudes A, noise amplitudes AN, SNR ratios A/AN, amplitude ratios with the FAF station and distance ratios with the FAF station.*

station	distance [km]	A	A_N	A/A_N	A_{FAF}/A	d/d_{FAF}
FAF	3.1	676.64	38.76	17.46	1.00	1.00
LAT	5.4	104.70	39.94	2.62	6.46	1.74
LSF	6.2	87.19	18.59	4.69	7.76	2.00
SEA	9.4	136.74	56.20	2.43	4.95	3.03
STH	10.7	46.93	14.67	3.20	14.42	3.45
LAG	10.9	40.31	19.13	2.11	16.79	3.52
ASH	12.5	47.18	14.50	3.25	14.34	4.03
KLV	15.4	35.28	21.70	1.63	19.18	4.97
LHL	23.5	44.19	32.80	1.35	15.31	7.58

The absolute tremor amplitudes showed a decreasing trend, when they were plotted against distance (Fig. 6.11). The biggest outlier was the SEA station, which was visibly stronger already in the tremor plot.

In finding the best fitting amplitude-distance relationship both the geometrical spreading and anelastic attenuation were taken into account. The attenuation coefficient α was computed using a grid search. When the FAF station was taken as a reference, the coefficient α was 0.4 using the L2 norm. A better result of α = 0.125 was obtained with a L1 logarithmic norm (Fig. 6.11). For the LAT station as a reference, the coefficient α was approaching zero. The same result was obtained with the STH station as a reference. The attenuation curve computed with $\alpha = 0$ intersected several stations, showing a good fit. The two outliers were the SEA and FAF stations. The other curve computed with $\alpha = 0.125$ also fitted amplitudes at few stations, but it was not representative for the others, showing them as outliers.

There were several solutions for the best fit, which varied based on the used norm and the chosen reference station. The computed geometrical spreading and anelastic attenuation combined together were not sufficient to account for all the different tremor amplitudes between stations.

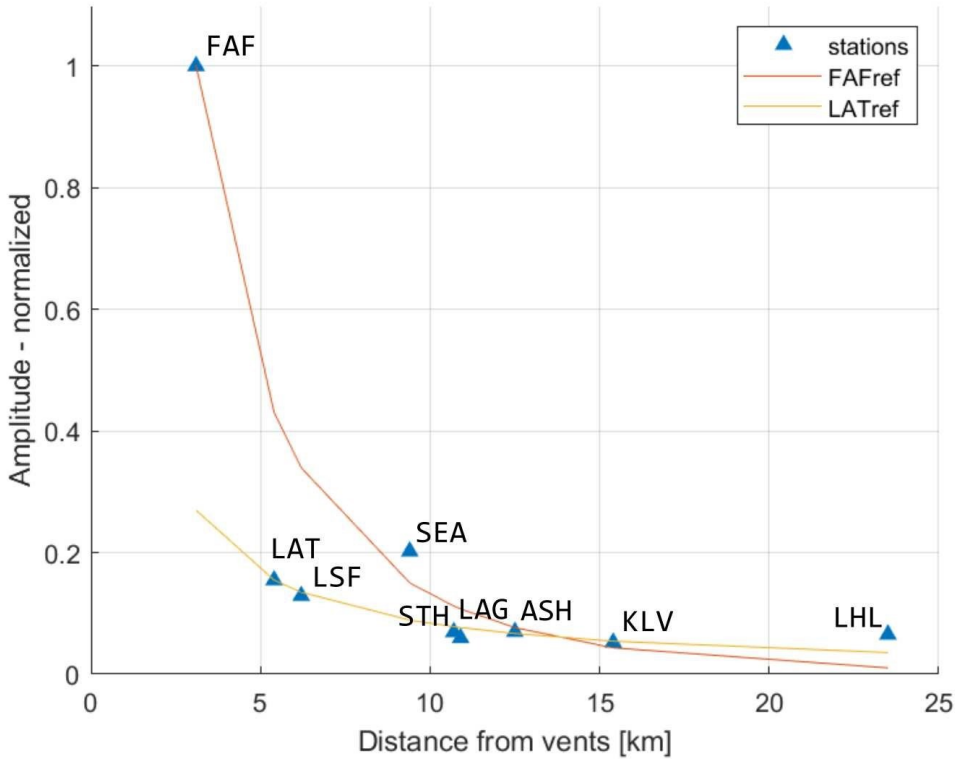

Figure 6.11: *Best fitting curves expressing the amplitude attenuation between stations. The L1 logarithmic norm and LAT as a reference station (yellow) showed a better fit than the same norm using FAF as a reference station (red).*

7 Discussion

The volcanic tremor during the 2021 Fagradalsfjall eruption showed similar characteristics to other documented cases. Its frequencies agreed with the 19 Hz range described by McNutt (1992), given the observed 1-10 Hz content at the FAF station. Also, the duration of individual tremors was in the expected range. The events spanned from the short 2-3 minute pulses in mid-May to the continuous 43 day long activity in early spring. Throughout the eruption, the frequency range did not substantially change at any station, which helped with the detection. All those characteristics have minimized the risk of analysing a tremor of non-volcanic origin.

A similar volcanic tremor was documented in Iceland by Benediktsdóttir et al. (2022) during the 2010 Eyjafjallajökull eruption. Its frequency range was broad, up to 10 Hz with spectral peaks detected at the closer stations. The 2010 tremor occurrence matched with the eruption, showing stronger signal during the effusive periods and weaker signal during the explosions (Benediktsdóttir et al., 2022). The tremor activity at Fagradalsfjall could be also matched with the different phases of the effusive eruption, as was suggested by Eibl et al. (2022). From the analysed time series and published information, it can be assumed, that the lava flow or another related process is responsible for the observed volcanic tremor.

The tremor onset was preceded and accompanied by an earthquake activity, which was possibly caused by the magma intrusions (Hobé et al., 2021). The activity reduced in the first weeks of the eruption, suggesting the incoming magma flow was directed into the existing open fissures, causing the dike propagation to cease. No major change in the tremor signal was seen during the opening of new fissures in the beginning of April, while the lava discharge rate remained relatively constant. The end of April was marked with high lava fountains reaching hundreds of meters, but the tremor strength did not increase. Also, from the observation of Eibl et al. (2022), the tremor amplitudes did not correlate with fissure openings or fountain heights.

The tremor changed from a continuous to a pulsating one on 2 May. The activity was confined to Vent 5, in which the lava level was fluctuating, reaching the top of the vent in the tremor peak periods (Eibl et al., 2022). Similar pulsations were observed during Kilauea eruption (Patrick, 2011) and in between geyser eruptions in Yellowstone (Nayak et al., 2020), where the tremor source was ascribed to the bubble collapse at the surface of the fluid. This seems like a reasonable explanation for the observed tremor pulses at Fagradalsfjall.

The regular pulsation lasted throughout May, exhibiting gradual increase in tremor amplitudes. This correlates with the increased lava discharge which has

risen from 7 to 12 m^3/s in May (Gudmundsson M. T. et al., 2021). The reason for a larger lava discharge during similarly long eruption periods could be the enlargement of the feeding channel.

Detail analysis of the pulses revealed changes in their periodicity. Their period was between 6 and 14 minutes, including the repose time. In the PSD spectra, there were visible frequency shifts, which seemed to negatively correlate with the amplitude changes (Fig. 6.8). If an unchanging repose time is assumed, the tremor pulses were getting longer and stronger, which agrees with the increasing lava discharge.

In the PSD spectra the pulses had no general shape, some exhibited sharper edges during onsets and endings than others. That was true at least for the shorter pulses in May and beginning of July, while the day-lasting pulses in August had gradual onsets and sharp endings (Appendix A). Therefore, it is probable that the course and mechanism of the two pulsating eruption types were different.

During June and July, the tremor amplitudes showed more irregular patter. On multiple occasions the tremor transitioned between continuous signal, pulsations and quiescence. One transition on 1 July was matched with a webcam recording of the Vent 5. It showed a continuous lava flow, which transitioned into pulsations. Then the activity decreased, as the lava surface started to drop in the vent (Vísir, 2021, 03:10). There is no clear explanation for those transitions, but multiple factors might play a role. This includes the magma composition and viscosity, changes in the feeding channel dynamics and its geometry.

The third and last tremor pattern observed during the Fagradalsfjall eruption were the highly regular day-lasting pulses in August. Their shape, duration, amplitude and frequency content showed minimum variation between individual events.

There was no gradual change in the tremor signal, that would precede or follow the long pulses. It can be speculated, that some transitional magma chamber might have started to control the course of the eruption.

In the half-year long series, the RMS amplitudes between LAT and FAF stations matched well in their shapes, showing high correlation coefficient for the periods of short pulses. This is consistent with the theory, that the volcanic tremor reflected the eruption process and not some minor local event near the FAF station.

The RMS amplitudes at FAF station were generally 6 times higher in comparison to the LAT station (Table 6.1), showing a substantial attenuation. The decrease in amplitudes was observed especially in the higher tremor frequencies between 5-10 Hz, which was consistent with Earth acting as a low-pass filter. That resulted in the delay of emerging tremor onsets at further stations. The computed

FAF/LAT ratio was not constant in this period, suggesting that the tremor signal at the LAT station did not exceed the noise level.

When plotted, the tremor amplitudes showed a decreasing trend with distance (Fig. 6.11). The SEA and FAF stations had higher amplitudes than expected and were the main outliers after plotting the best fitting attenuation curve. In case of the SEA station, the tremor signal might have been stronger due to the increased noise level in the tremor frequency range. The station is positioned on the southern coast, where the seismic noise, caused by the wind and sea is relatively strong.

At the FAF station, the higher amplitudes were more difficult to explain, because its SNR ratio was the highest among stations. The anelastic attenuation did not seem to have a major effect with the attenuation coefficient being around 0 for the best fitting curves. Therefore, it could not explain the substantial amplitude difference between the FAF and the far stations. One possible explanation could be, that the assumed source location was different. In this scenario, the source would be closer to the FAF station, than originally assumed.

Fischer et al. (2021) described the propagation of a 10-km long regional dike prior to the eruption, which was accompanied by earthquakes. According to Benediktsdóttir et al. (2022), the dike was elongated in SWNE direction spanning from Fagradalsfjall to Keilir, not far from the FAF station. The depth of the dike between 0.5-2 km below the surface would also have to be taken into account (Gudmundsson A. et al., 2021). Although such source seems plausible, a shift into a deeper location would imply a different trigger mechanism of the tremor, than a burst of bubbles in the feeding channel. There is not enough evidence to support or rule out this hypothesis and a better estimate of the source would have to be computed using location methods.

Another influence to attenuation analysis and amplitude differences between stations are the inhomogeneities and various boundaries in the subsurface. The seismic signal must cross several SW-NE trending fissures and faults before arriving at the LAT station. Because the FAF station is in the general fissure direction from the source, the signal arrives less distorted and stronger, which results in the higher amplitudes at this station.

8 Conclusion

The conducted analysis of tremor signal during the 2021 Fagradalsfjall eruption showed several interesting outcomes.

The volcanic tremor was present during the whole eruption from March to September and matched with the times of effusive activity. The bubble burst of magma at the top of the feeding channel of the main vent was considered to be triggering the tremor signal. but more detailed analysis would be necessary to determine the true location.

While the tremor frequency content and location seemed invariable with time, there were substantial changes in amplitude. The tremors had emerging onsets, suggesting gradual increase of activity in the source, while their endings were sharp and abrupt.

Three main patterns were detected, including a continuous tremor prevailing in the beginning of the eruption. Short time pulses were typical in the middle stage and long-time pulses marked the ending of the eruption. In May, the tremor amplitudes substantially increased, which matched with the observed increase of lava discharge. The exact reason of those variations is not known, but presumably reflects the changes in geometry and magma flow in the underground magmatic system.

The attenuation analysis showed a decrease of amplitudes with distance, but also great variability between stations, that could not be explained by geometrical spreading nor by anelastic attenuation. In order to explain these results and narrow down the uncertainties, an analysis using data from more stations and days would be necessary.

The 2021 Fagradalsfjall eruption attracted many scientists worldwide, which means it was thoroughly documented in real time. The presented study with the use of those observations helps to understand the underlying processes of volcanic eruptions and their seismic signatures. It can be a valuable finding in case of more remote eruptions, that are not observed in situ, but still appear on the seismic recordings. Also it can help studies, which focus on modelling the tremor sources and describing the trigger mechanisms.

References

Ahern, T., R. Casey, D. Barnes, R. Benson, T. Knight, and C. Trabant (2009): SEED Reference Manual, version 2.4, Incorporated Research Institutions for Seismology (IRIS), Retrieved from: http://www.fdsn.org/seed_manual/SEEDManual_V2.4.pdf

Alsadi, H. N. (2016): Seismic Hydrocarbon Exploration: 2D and 3D Techniques. Springer. 331 pp., ISBN: 3319404369.

Benediktsdóttir, Á., Gudmundsson, Ó., Li, K. L. and Brandsdóttir, B. (2022): Volcanic tremor of the 2010 Eyjafjallajökull eruption. Geophysical Journal International, Vol. 228, No 2, 1015-1037.

Beyreuther, M., Barsch, R., Krischer, L., Megies, T., Behr, Y., and Wassermann, J. (May/June 2010): ObsPy: A Python Toolbox for Seismology, Seismological Research Letters, Vol. 81, No 3, 530-533.

Blanck, H., Jousset, P., Hersir, G.P., Ágústsson, K. and Flóvenz, Ó.G. (2020): Analysis of 2014-2015 on-and off-shore passive seismic data on the Reykjanes Peninsula, SW Iceland. Journal of Volcanology and Geothermal Research, Vol. 391, 106548.

Bormann, P. and Wielandt, E. (2002): Chapter 4 - Seismic signals and noise. IASPEI New manual of seismological observatory practice, GeoForschungsZentrum Potsdam, 62 pp.

Cerna, M., and Harvey, A.F. (2000): The fundamentals of FFT-based signal analysis and measurement. Application Note 041, National Instruments.

Eibl, E. P., Lokmer, I., Bean, C. J., Akerlie, E. and Vogfjörd, K. S., (2015): Helicopter vs. volcanic tremor: Characteristic features of seismic harmonic tremor on volcanoes. Journal of Volcanology and Geothermal Research, Vol. 304, 108-117, ISSN 0377-0273.

Eibl, E. P., Bean, C. J., Jónsdóttir, I., Höskuldsson, A., Thordarson, T., Coppola, D., Witt, T. and Walter, T. R. (2017): Multiple coincident eruptive seismic tremor sources during the 2014Ű2015 eruption at Holuhraun, Iceland. Journal of Geophysical Research: Solid Earth, Vol. 122, No 4, 2972-2987.

Eibl, E. P. S., Thordarson, T., Hoskuldsson, A., Gudnason, E. A., Dietrich,T., Hersir, G. P., Agustsdottir, T. (2022): Evolving Shallow-conduit Container Affects the Lava Fountaining during the 2021 Fagradalsfjall Eruption, Iceland, in review.

Everett, M. E. (2013): Near Surface Applied Geophysics, Cambridge University Press, pp. 403, ISBN: 1107018773, 9781107018778.

Fischer T., Hrubcová P., Salama, A., Doubravová, J., Ágústsdóttir T., Gudnason E. Á., Horálek, J., Hersir, G. P. (2022). Swarm seismicity illuminates stress transfer prior to the 2021 Fagradalsfjall eruption in Iceland, EPSL, in review.

Global Volcanism Program (2013): Volcanoes of the World, v. 4.10.6 (2022). Venzke, E (ed.). Smithsonian Institution.

Gudmundsson, A., Bazargan, M., Hobé A., Selek, B., Tryggvason, A., Sil Seismological Group (2021): Dike-segment propagation, arrest, and eruption at Fagradalsfjall, Iceland. AGU Fall Meeting, 13 Decemer, New Orleans.

Gudmundsson, M. T., Halldórsson, S. A., Belart, J. M. (2021): Eldgos í Fagradalsfjalli. Retrieved from: http://jardvis.hi.is/eldgos_i_fagradalsfjalli

Hobé, A., Selek, B., Bazargan, M., Tryggvason, A., Gudmundsson, A. (2021): Using seismicity and tomographic imaging to infer the location and rupture of the reservoir that supplies magma to the 2021 eruption at Fagradalsfjall, Iceland, AGU Fall Meeting, 13 December, New Orleans.

Hotovec, A.J., Prejean, S. G., Vidale, J.E. and Gomberg, J. (2013): Strongly gliding harmonic tremor during the 2009 eruption of Redoubt Volcano. Journal of Volcanology and Geothermal Research, Vol. 259, 89-99.

Hrubcová, P., Doubravová, J. and Vavryčuk, V. (2021): Non-double-couple earthquakes in 2017 swarm in Reykjanes Peninsula, SW Iceland: sensitive indicator of volcano-tectonic movements at slow-spreading rift. Earth and Planetary Science Letters, Vol. 563, 116875.

Hurst, A.W., (1992): Stochastic simulation of volcanic tremor from Ruapehu. Journal of volcanology and geothermal research, Vol. 51, No 3, 185-198.

Icelandic Met Office (2022): Earthquake swarm on the Reykjanes Peninsula. [online]. (Last updated 5 January 2022). Available at: https://www.vedur.is/um-vi/frettir/ jardskjalftahrina-a-reykjanesskaga[Accessed 27 March 2022].

Kayal, J. R. (2006): Earthquakes magnitude, intensity, energy, power law relations and source mechanism. Geological Survey of India. Retrieved from: https://escweb.wr.usgs.gov/share/mooney/SriL.II3.pdf

Kedar, S., Sturtevant, B. and Kanamori, H. (1996): The origin of harmonic tremor at Old Faithful geyser. Nature, Vol. 379, 708-711.

Konstantinou, K. I. and Schlindwein, V. (2003): Nature, wavefield properties and source mechanism of volcanic tremor: a review. Journal of Volcanology and Geothermal Research, Vol. 119, No 1-4, 161-187.

Krischer, L., Megies, T., Barsch, R., Beyreuther, M., Lecocq, T., Caudron, C., and Wassermann, J. (2015): ObsPy: a bridge for seismology into the scientific Python ecosystem, Computational Science & Discovery, Vol. 8, No 1.

Lowrie, W. (2007): Fundamentals of Geophysics, Second Edition, Cambridge University Press, ISBN: 1139465953, 9781139465953.

McNutt, S. R. (1992): Volcanic tremor. Encyclopedia of earth system science, Vol. 4, 417-425.

Nayak, A., Manga, M., Hurwitz, S., Namiki, A. and Dawson, P. B. (2020): Origin and properties of hydrothermal tremor at Lone Star Geyser, Yellowstone National Park, USA. Journal of Geophysical Research: Solid Earth, Vol. 125, No 12.

Patrick, M.R., Orr, T., Wilson, D., Dow, D. and Freeman, R. (2011): Cyclic spattering, seismic tremor, and surface fluctuation within a perched lava channel, K'ılauea Volcano. Bulletin of volcanology, Vol. 73, No 6, 639-653.

Permana, T., Nishimura, T., Nakahara, H. and Shapiro, N. (2022): Classification of volcanic tremors and earthquakes based on seismic correlation: application at Sakurajima volcano, Japan. Geophysical Journal International, Vol. 229, No 2, 1077-1097.

Sæmundsson, K., Sigurgeirsson, M.Á. and Friðleifsson, G.Ó. (2020): Geology and structure of the Reykjanes volcanic system, Iceland. Journal of Volcanology and Geothermal Research, Vol. 391, 106501.

Schafer, R.W. (2011): What is a Savitzky-Golay filter?[lecture notes]. IEEE Signal processing magazine, Vol. 28, No 4, 111-117.

Schlindwein, V., Wassermann, J. and Scherbaum, F. (1995): Spectral analysis of harmonic tremor signals at Mt. Semeru volcano, Indonesia. Geophysical research letters, Vol. 2, No 13, 1685-1688.

Shearer, P. M. (2019): Introduction to seismology. Cambridge university press, 396 pp., ISBN: 0521882109.

Smith, J. O. (2007): Mathematics of the Discrete Fourier Transform (DFT) with Audio Applications, Second Edition, W3K Publishing, 306 pp., ISBN 978-9745607-4-8.

Teupser, C. and Plešinger, A. (1979): Design of feedback-controlled wide-band seismographs with respect to undesired side-effects. Physics of the Earth and Planetary Interiors, Vol. 18, No 2, 58-63.

Vísir (2021): Eldgígurinn lagðist í dvala í gærkvöldi. 6 July. Available at: https://www.visir.is/g/20212130255d. [Accessed: 27 March 2022]

Yukutake, Y., Honda, R., Harada, M., Doke, R., Saito, T., Ueno, T., Sakai, S.I. and Morita, Y. (2017): Analysing the continuous volcanic tremors detected during the 2015 phreatic eruption of the Hakone volcano. Earth, Planets and Space, Vol. 69, No 1, 1-16.

Zobin, V. M. (2003): Introduction to Volcanic Seismology, First edition. Elsevier Science, Amsterdam-New York-Tokio, 482 pp., ISBN: 0-444-51340-X.

Appendix A

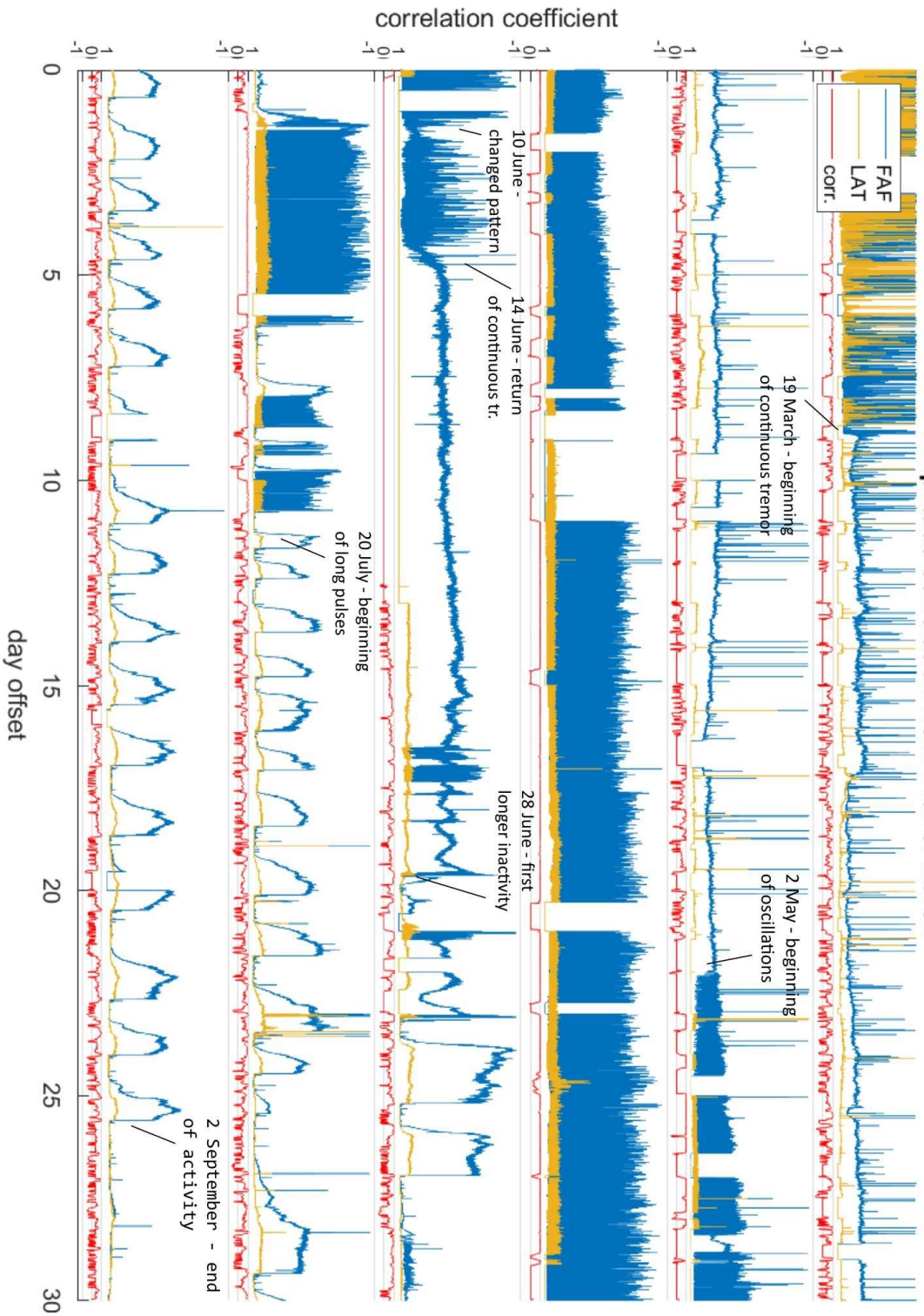
Amplitude correlation from 11th of March
correlation coefficient
FAF
LAT
corr.
19 March - beginning of continuous tremor
2 May - beginning of oscillations
10 June - changed pattern
14 June - return of continuous tr.
28 June - first longer inactivity
20 July - beginning of long pulses
2 September - end of activity
day offset
0
5
10
15
20
25
30